Garnet pyroxenites explain high electrical conductivity in the East African deep lithosphere

Thomas P. Ferrand, Emily Chin

Garnet pyroxenites explain high electrical conductivity in the East African deep lithosphere

Thomas P. Ferrand[1,2] & Emily J. Chin[3]

1: Institut für Geologische Wissenschaften, Freie Universität Berlin, Malteserstraße 74-100, Berlin 12249, Germany

2: Institut des Sciences de la Terre d'Orléans, CNRS UMR 7327, Université d'Orléans, France;

3: Geosciences Research Division, Scripps Institution of Oceanography, UC San Diego, La Jolla, USA.

Contact: *thomas.ferrand@fu-berlin.de*

Abstract

In Tanzania, the deep lithospheric mantle (> 70 km depth) is characterized by significantly higher electrical conductivity within the cratonic root than in the Mozambique belt. Such contrasts are typically attributed to changes in volatiles and/or melt content, with changes in mineralogy deemed insufficient to impact conductivity. To test this assumption, electrical conductivity measurements were conducted at pressure-temperature conditions relevant to the Tanzanian lithosphere (1.5 and 3 GPa; from 400 to > 1500°C) on dunite (depleted) and pyroxenite (fertile) xenoliths from Engorora, Northern Tanzania. Once garnet becomes stable in the fertile mantle rock (> 60 km, 1.7 GPa), it nucleates at grain boundaries, forming the backbone of a conductive network. At 3 GPa, such garnet-rich networks increase conductivity by a factor of 100 regardless of temperature. Numerical models demonstrate that the observed low (< 10^{-2} Sm^{-1}) and high (> 10^{-1} Sm^{-1}) conductivity values can be explained by low and high degrees of garnet connectivity, respectively. Such high electrical conductivities in cratonic roots can be explained by the presence of connected garnet clusters or garnet pyroxenites, suggesting mantle fertilization. This new source for electromagnetic signal generation at appropriate pressures and temperatures must be factored in where interpreting magnetotelluric signals at relevant depths in the lithosphere.

Keywords: **Craton, Mantle, Tanzania, Garnet pyroxenite, Lithosphere, Electrical conductivity.**

Key Points:

- **Electrical conductivity measurements at high pressures and temperatures were conducted on dunite and pyroxenite xenoliths from Tanzania.**
- **The high electrical conductivity is associated with networks of garnet pyroxenites, with natural H contents limited < 0.1 vol.%.**
- **The high electrical conductivity in the root of the Tanzanian Craton would highlight current plume impingement.**

Plain Language Summary

The deep root of the Tanzanian craton is characterized by high electrical conductivity. In this study, we reproduce this anomaly in the laboratory. We use powders of Tanzanian xenoliths, which are natural rocks similar to what is expected in the deep Tanzanian lithosphere. Two extremes of mantle composition are tested: dunite and pyroxenite, respectively typical of a depleted mantle (already produced melts) and fertile mantle (high chemical diversity). Experiments at high pressures and temperatures representative of the deep Tanzanian lithosphere reveal that the high electrical conductivity is generated by the establishment of a connected network of garnet pyroxenites. Minerals such as garnet and pyroxenes are known to conduct electricity much better than olivine – the major component of most mantle rocks – especially when they contain limited amounts of hydrogen. This "water" is incorporated in crystals and at their boundaries and promotes high-conductivity pathways. A significant increase in conductivity occurs once the pressure is high enough for garnet to become stable. These results suggest that the composition of the deep cratonic root in Tanzania is closer to a pyroxenite than a peridotite. This difference in composition compared to the average mantle is expected as an impact of the East African superplume.

1. Introduction

The structure and composition of the cratonic lithosphere has been debated for decades (e.g. Takahashi, 1990; Evans et al., 2011) but these deep regions of the Earth are only directly accessible via volcanically-derived xenoliths (e.g. Henjes-Kunst & Altherr, 1992; Vauchez et al., 2005; Doucet et al., 2014; Chin, 2018) and through indirect geophysical imaging (e.g. O'Donnell et al., 2013; Selway, 2015; Sarafian et al., 2018). The formation of cratons and their evolution through time are still under investigation (e.g. Liu et al., 2021), particularly their apparent longevity, although focus is also turning to processes of plume impingement that might eventually trigger craton disruption (Griffin & O'Reilly, 2007; Foley, 2008; Wang et al., 2015; Koptev et al., 2016). Magnetotellurics (MT) offers a powerful approach to understanding the structure of the lithosphere and upper mantle. For example, several studies report anomalously high conductivities in the lithospheric mantle, notably below the East African Rift (**Fig.1**; Selway, 2015; Sarafian et al., 2018). These anomalies are thought to provide evidence for the presence of volatiles and/or the occurrence of melting at depth (Selway, 2015).

A high-conductivity anomaly (> 10^{-2} Sm^{-1}) is observed below the Tanzanian Craton at depths > 70 ±10 km, while the conductivity of the neighboring Mozambique Belt at the same depth is much lower (< 10^{-3} Sm^{-1}; Selway, 2015). The contrast between the cratonic root and the mobile belt is striking, and counter to

almost all observations in other similar tectonic settings (e.g. Evans et al., 2011; Sarafian, 2018). Selway et al. (2014) hypothesized that the high conductivity of the cratonic lithosphere is caused by the presence of water dissolved in olivine. However, this explanation contradicts models of cratonic root formation that consider predominantly depleted and dry roots. Furthermore, volatiles are known to lower mantle viscosity, enhancing the likelihood of mantle deformation (Hirth & Kohlstedt, 2003), which would not be consistent with craton stability. Most xenoliths have revealed that the non-metasomatized cratonic lithosphere is characterized by low bulk H content (~20-30 ppm H_2O; Peslier et al., 2017), but this field is currently debated and methods evolve rapidly. Partly destroyed cratons such as the North China craton (NNC) can exhibit highly variable H contents, ranging from 10-100 ppm (northern NCC; Chin et al., 2020) up to 2900 ppm H_2O (eastern NNC; Wang et al., 2022). The limited H contents observed in Kaapvaal xenoliths (South Africa) are consistent with observed low conductivities (Evans et al., 2011; Jones et al., 2012). In addition, pyroxenites from Hawaii, located over a mantle plume, are 4 times more hydrated than typical oceanic mantle (Bizimis & Peslier, 2015), which suggests that plume impingement could also increase the water content of cratonic roots. Yet, fertilization processes may depend on geological settings and would not necessarily require the action of a mantle plume (Griffin et al., 2009; O'Reilly & Griffin, 2013).

To probe the origin of electrically-conductive cratonic environments, we experimentally reproduced the pressure-temperature conditions relevant to the deep Tanzanian lithosphere and performed electrical measurements on xenoliths from the area. The xenoliths originate from Engorora, Northern Tanzania (Chin, 2018). We used powders of a clinopyroxenite (ENG7) and a dunite (ENG8), two endmember lithologies in the area (Chin, 2018), hereafter referred to as fertile and depleted compositions, respectively (**Tables 1** and **2**).

2. Material and methods

2.1. Starting Material: description, significance and representativity

The Engorora xenoliths (Chin, 2018) consist of clinopyroxenites, wehrlites and dunites. In this study we used powders of a clinopyroxenite (ENG7) and a dunite (ENG8), which can be considered as two endmember mantle lithologies, hereafter referred to as fertile and depleted, respectively. Based on modal analysis and petrography from Chin (2018), ENG7 has 87% clinopyroxene, 11% orthopyroxene, 2% olivine, and trace amounts of chromite. Texturally, ENG7 has a poikilitic texture with clinopyroxene oikocrysts enclosing olivine and orthopyroxene chadacrysts. In general, grain size of the clinopyroxenite endmember xenoliths is variable and ranges from 1 mm to >5 mm. The clinopyroxenites do not show recrystallization

or other evidence of tectonic deformation. The dunite endmember xenoliths have a modal mineralogy of 95% olivine, 4% clinopyroxene, and ~1% chromite. In contrast to the clinopyroxenites, the dunites have a very coarse-grained (~5 mm) and equigranular texture, and clinopyroxene, where present, is typically anhedral and often occurs interstitially between olivine grains.

Engorora, Chyulu (Southern Kenya) and the Lashaine area (10 km to the west from Engorora), are characterized by a large diversity of ultramafic xenoliths, including pyroxenites, lherzolites, harzburgites, wehrlites and/or dunites, the recorded depth of which depending on local specificities of volcanic systems (sampling depth). The magma ascent bringing xenoliths to the surface via volcanic eruptions involves percolation thresholds and local geological specificities, which lead to different sampling depths. For instance, the Engorora xenoliths contain spinel (Chin, 2018), while Chyulu exhibits mantle xenoliths containing connected garnet networks (Henjes-Kunst & Altherr, 1992), which does not mean that the Chyulu mantle would have more garnet on average. At depths >70 km, the lithospheric mantle contains garnet, but its amount and distribution can be highly variable (e.g. Lee & Rudnick, 1999).

The powders used in this study come from two endmembers of Engorora xenoliths. They present similar particle size distributions, with mean values of about 12 and 9 μm, respectively (**Fig.S1**). Chemical compositions of ENG7, ENG8 and their host lava are provided in **Table 1**, along with compositions of their equivalent in Lashaine (Dawson et al., 1970) and of mantle rocks from a previous electrical conductivity study in China (Wang et al., 2008). The mineralogy and H contents of the Engorora xenoliths are provided in **Table 2**. Further details are listed in the ***Supplementary Information*** (***section 1***), including carbon content (**Fig.S2**) and water content (**Fig.S3**) estimates.

2.2. Experimental protocol

All powders were stored in a desiccator to avoid water adsorption. Prior to experiments, the MgO parts of the assembly were fired to 1100°C during one hour and stored in a desiccator as well.

High-pressure, high-temperature experiments have been conducted using the 14/8 COMPRES electrical assembly (**Fig.2**) designed for electrical conductivity measurements in the multi-anvil (Pommier & Leinenweber, 2018). Each experiment was performed at a fixed pressure and the electrical conductivity was measured with increasing temperature, up to temperatures between 1400 and 1550°C depending on the experiment. The experimental conditions are summarized in **Table 3**, including available data on water and carbon contents, respectively estimated using SIMS and Raman measurements on the xenoliths from which the powders originate**.** An example of recovered quenched sample is presented in **Fig.3**.

Each experiment on peridotites and pyroxenites reported in this study has been performed with the same protocol (**Table S1**). First, pressure was increased from atmospheric pressure to the target pressure

over several hours, then temperature was increased from room temperature to ≈ 400°C for a short dwell to achieve electrical equilibrium. The temperature was then lowered to < 300°C in order to start the experiment on an equilibrated system. Electrical measurements are then collected during heating until the sample is quenched at the highest T, except BB-238, for which a slow decrease of temperature was imposed after the peak temperature. Overall, the entire heating procedure until the target T of ≈ 400°C is reached and stable takes about 1h. During experiment BB-246, some instability in electrical measurements was noted upon heating (T < 800°C) after the dwell, and consequently the additional experiment BB-254 was performed. Such instability is interpreted as due to high-pressure transformations at grain boundaries in light of kinetics considerations (as confirmed by microstructural observations, ***section 3.2***).

To ensure reproducibility, experiment BB-246 has been reproduced with experiment BB-254 (**Table 3**). An additional experiment (BB-253) was performed on the pyroxenite powder up to 750°C only, i.e. quenched before any partial melting could occur, in order to check which microstructure was responsible for the drastic pressure-induced change in the conductivity values. No conductivity data were measured during this experiment. A summary of the experiments is provided in **Table 3**. The experimental conditions are illustrated on **Fig.4**, which also summarizes thermodynamic equilibrium of typical mantle peridotites and pyroxenites. Electrical conductivity and temperature measurements, with associated uncertainties, are described in the ***Supplementary Information*** (***section 2***).

3. Results

3.1. Microstructural analyses

Retrieved assemblies were cut along the furnace and polished using sandpaper and diamond paste down to 1 µm. Microstructures (**Fig.5** to **9**) were imaged using a scanning electron microscope (SEM) at UCSD, Nanoengineering Facility. Mineral composition (**Table S2**) and element mapping (**Fig.S5** and **Fig.S6**) were acquired using energy dispersive X-ray spectroscopy (EDS).

In experiments performed at 3 GPa, microstructural observations reveal numerous garnet crystals, preferentially residing in the grain-boundary network of the pyroxenite samples (**Fig.5**); in the dunite samples sintered at 3 GPa, garnets are scarce and isolated (**Fig.8**). In contrast, for experiments on pyroxenites that reached 1.5 GPa only, microstructural observations do not reveal garnet growth but apparently stable Al-rich spinel (**Fig.9**). Some isolated grains of accessory phases are also observed in the samples (e.g. chromite, hibonite, metal alloys) but the spinel-garnet transition (≈ 1.8 GPa in lherzolites) is the major metamorphic transformation in these conditions.

Counting pixels using *Adobe Photoshop* on **Fig.5b** (3 GPa; ≤ 1400°C), the modal abundance of garnet is estimated to be a few percent, e.g. ~5 vol.% for run BB-246. A similar analysis on **Fig.7a** (large garnet cluster around metal-rich inclusions) gives garnet fraction estimates of 7-8 vol.%, but the occurrence of local clusters cannot significantly increase the overall connectivity of the conductive garnet-rich network.

3.2. Electrical conductivity

At 1.5 GPa (≈50 km depth) and over the investigated temperature range, the pyroxenite and dunite samples present similar conductivity values. These values would agree with a moderate bulk hydration (~100 ppm; Wang et al., 2006; Yang et al., 2011; Gardés et al., 2014), relative to typical cratonic mantle (Peslier et al. 2017). At 3 GPa (≈ 100 km depth), dunite conductivity decreases by a factor ranging from 10 to 100, depending on temperature (**Fig.10a**), whereas pyroxenite conductivity increases by a factor of about 10. The results at 3 GPa are in relatively good agreement with conductivities reported previously for dunite, lherzolite and pyroxenite containing minor H amounts (~ 100 ppm H_2O), showing that pyroxenites are significantly more conductive (Wang et al., 2008), although less conductive than the Engorora pyroxenite xenolith (ENG7; **Fig.10a**). At high temperature (1300°C) the latter is as conductive as a silicate melt with moderate hydration (0.2 – 1 Sm^{-1}). According to SIMS measurements on cores of olivine and pyroxene crystals, the ENG7 and ENG8 samples contain at least moderate H amounts, but hydration alone cannot explain the contrast between the measured conductivity from 1.5 to 3 GPa (Dai et al., 2012; Gardés et al., 2014). The electrical transition between 1.5 and 3 GPa would therefore be due to garnet nucleation.

Because electrical conductivity provides information about the connectivity of conductive phases (Glover et al., 2000; Wang et al., 2013; Miller et al., 2015), the conductivity results (**Fig.10a**) are presented together with a range of connectivity models (**Fig.10b**) further described in ***section 4***. These models assume diverse geometrical distributions of the conductive network within the samples, and are not scale dependent, which allows upscaling our results following representativity assumptions formulated and discussed in ***sections 4*** and ***5***. In **Fig.10b**, the conductivity results at 600°C and 800°C are compared to the connectivity models, which allows us to estimate the expected amount (volume fraction) of the conductive network that is required in these models to explain the recorded electrical data.

3.3. Garnet-rich networks as a plausible candidate to explain high electrical conductivity

Microstructural observations illustrate that the electrical transition correlates with the nucleation of garnet, preferentially residing in the grain-boundary network of the pyroxenite samples (**Fig.5**). Electrical conductivity data suggest that the garnet pyroxenite network observed at 3 GPa in the pyroxenite is highly conductive (> 10^{-2} $S.m^{-1}$ at T > 750°C, **Fig.10a**). Iron increases garnet conductivity (Dai et al., 2012), due to the decrease of the average distance between Fe^{2+} and Fe^{3+} (Romano et al., 2006). It should be noted that

similar values are obtained if the garnet composition is ~Py_{73}-Alm_{14}-Grs_{13} (≈ 5.6 wt.% Fe; Dai et al., 2012) and Py_{85}-Alm_{15} (≈ 6 wt.% Fe; Romano et al., 2006). Despite the small size of the nucleated garnet crystals in the recovered samples, an approximate formula of ~Py_{51}-Alm_{18}-Grs_{31} (≈ 6.9 wt.% Fe) is obtained using EDS measurements (**Table S2; Fig.S5** and **S6**). Since garnet is surrounded by Fe-poor, Ca-rich clinopyroxenes, the almandine fraction (Alm) represents a compositional lower bound (i.e. the garnet iron content is ≥ 6.9 wt.%). Nonetheless, the conductivity of dry Py_{20}-Alm_{76}-Grs_{4} (≈ 26.7 wt.% Fe) garnet does not exceed 10^{-3} $S.m^{-1}$ at 850°C (Dai et al, 2012), which is 100 times lower than the measured bulk conductivity value (**Fig.10b**). Therefore, the high conductivities of the pyroxenite samples cannot be solely attributed to the iron content of the garnet. Including minor water within garnets and pyroxenes could, however, reproduce the observations. The conceptualization and extrapolation to nature is provided in ***section 4*** and ***section 5***, respectively.

The presence of garnet, expected according to both thermodynamics, is evidenced by microstructural observations (***section 3.2***) of samples retrieved after experiments at 3 GPa (**Fig.5** to **Fig.S6**). In various natural lithologies, garnet is reported as preferentially distributed in layers or channels (***section 4.1***); in our experiments, garnet, which represents some vol.% at 3 GPa (up to ~5 vol.% in **Fig.5b**), is preferentially distributed along grain boundaries, where reactive phases are in contact (***section 4.2***) and where diffusivity is enhanced (Fisher, 1951). Garnet networks have been observed in xenoliths (Henjes-Kunst & Altherr, 1992) in the same region (Chyulu, Southern Kenya; **Fig.S7a**, located in **Fig.1**), which can be seen as an analogue of the experimental garnet-rich networks. Thus, the experiments at 3 GPa would be representative of larger-scale natural features and we argue that their bulk electrical response is relevant to interpret the deep conductive anomaly.

The electrical data highlight a transition in the electrical response of the pyroxenite and dunite samples between 1.5 and 3 GPa, respectively characterized by an increase and a decrease in conductivity. Both xenoliths contain minor carbon impurities located at grain boundaries (**Fig.S2**), consistently with the literature (Watson, 1986; Pearson et al., 1994), which would be consistent with the CO_2-rich magmatism observed in the area and oxygen fugacity considerations (***Discussion***). Solid carbon (either graphite or amorphous carbon) is known to be highly conductive (~10^{5} $S.m^{-1}$; Duba & Shankland, 1982) and thus significantly enhance conductivity when connected (≥ 1 wt.%; Wang et al., 2013). However, a recent study revealed that carbon grain-boundary films are not stable at upper-mantle pressures (reductive conditions) and that carbon is thus unlikely to explain the high-conductivity anomalies revealed by MT surveys in the upper mantle (Zhang & Yoshino, 2017). In addition, there is no reason for carbon to become more

conductive/connected with increasing pressure. Consequently, the presence of carbon alone is insufficient to explain the data.

In the experiments reported in this study, the increase of conductivity is limited to pyroxenites because in dunites (i.e. > 90% olivine) the connectivity of the (rare) conductive minerals is close to zero. However, in nature, mantle rocks such as foliated lherzolites could well be as conductive as garnet pyroxenites, as long a relatively dense conductive network exists and is connected (see conceptualization in ***section 4*** and discussion in ***section 5***).

4. Conceptualization and forward modelling

4.1. Widespread hydrous garnets and pyroxenes in the mantle

Although water is widely reported to be incorporated into pyroxenes (~ 100 ppm), garnet can also accommodate a significant H amount in its crystal lattice (~ 1000 ppm H_2O; Aines & Rossman, 1984; Maldener et al., 2003). A review of limited (≈ 500 ppm H_2O) to high (≈ 2500 ppm H_2O) amounts of hydrogen in natural garnets is provided by Ferrand (2020). The garnet identified in this study (3 GPa) has the approximate formula ~Py_{51}-Alm_{18}-Grs_{31}, which is, considering the explanations hereabove, ideal for hydrogarnet stability. The high affinity of garnet and pyroxene crystals for hydrous defects (e.g. hydrogarnet) should lead high H contents in the microcrystalline grain-boundary paragenesis. Consistently with recent reviews (e.g. Peslier et al., 2017) and with the high affinity of garnet for hydrous defects compared to other mantle minerals, we consider water contents of the garnet pyroxenite networks between 50 and 500 ppm.

Electrically, water in garnet significantly increases conductivity; for instance, hydrous pyrope (with 465 ppm H_2O) is 100 times more conductive at 750°C than its anhydrous counterpart (**Fig.10b**; Dai et al., 2012). The only studies that have investigated the electrical conductivity of hydrous garnets used a pyrope from Garnet Ridge, Arizona, USA, of composition ~Py_{73}-Alm_{14}-Grs_{13} (Dai & Karato, 2009; Dai et al., 2012), with H contents of 465, 160 and 46 ppm H_2O. A value of 465 ppm is assumed in **Fig.10** and **Fig.11**. The impact of H content on the simulations is addressed in **Fig.12**.

In ***section 5***, electrical anomalies in the deep Tanzanian lithosphere are reappraised in light of our experimental results (**Fig.13**). Two endmember scenarios are considered, depending on the amount and connectivity of garnets: the deep Tanzanian lithosphere is composed of either (1) fertile mantle rocks with garnet-rich networks or (2) depleted mantle rocks without garnet-rich networks.

4.2. Garnet pyroxenite formation and connectivity

Reaction kinetics is key in the development of metarmorphic microtextures (Ridley & Thompson, 1986). Studies have reported garnet nucleation and growth at low temperatures (Lanari & Engi, 2017 and references therein). Notably, garnet crystals (5 mm average diameter) are reported in the southern Omineca belt of the Canadian Cordillera, which underwent Barrovian metamorphism peaking at middle amphibolite facies during the Early Cretaceous. Garnet porphyroblasts grew along a P-T path from 500°C at 0.5 GPa to 570°C at 0.7 GPa. For comparison, in experiment BB-253 (≤ 750°C, 3 GPa), submicrometric garnet crystals grew at grain boundaries in less than 2 hours at T > 400°C.

Most experimental petrology experiments focus on high temperatures for two reasons: 1) in nature, garnet nucleation and growth at T < 500°C in ultramafic rocks is rather unrealistic, and 2) high temperatures are required for grain growth to occur fast enough during an experiment in order to perform single-grain analyses with various techniques.

Polymorphic transformations such as the quartz-coesite transition can easily occur at low temperatures because it requires no or limited atomic diffusion. Contrastingly, the "spinel-garnet transition", i.e. transition from a spinel lherzolite/pyroxenite to a garnet lherzolite/pyroxenite, is a metamorphic reaction involving the reorganization of several phases within a paragenesis, i.e. at the scale of several grains (e.g. Lanari & Engi, 2017, and references therein). For such metamorphic reaction, the thermodynamics is highly impacted by kinetics, which allows at low temperatures the preservation of metastable HP-HT rocks eventually exposed to the surface after the erosion of internal mountain belts. Especially, any reaction that involves garnet formation involves Al^{3+} diffusion, which is slow at 800°C.

Another parameter controlling reaction kinetics is thermodynamic overstepping, which is a driving force that is necessary for porphyroblast nucleation and growth (Spear, 2017). The growth of nanometric garnets likely initiated during the initial sintering process. At such low temperatures, the reaction occurred only where the reactive minerals are close to each other, i.e. at grain boundaries. Although Al^{3+} intracrystalline diffusion is slow, we consider that the original garnet-rich network in the samples at temperatures between 400 and 800°C is the result of the small grain size and favoured contacts between the reactive minerals during initial heating and powder compaction. Considering a Stefan's interface model for garnet growth, the growth of crystals at 700°C up to a radius of 10 or 100 nm is feasible in a few minutes and a few hours, respectively (Spear, 2017; Mg-poor system). Some garnet grains are larger (up to ≈ 1 µm in radius at 750°C; **Fig.S6**), which can be due to both the large pressure overstep (ΔP > 1 GPa; **Fig.4**) and larger diffusivity in Mg-rich systems compared to Mg-poor systems.

The garnet-rich network developing at grain boundaries is an example of local mineral assemblage due to slow metamorphic reactions within the intergranular system, referred to as grain-boundary equilibrium

(Lanari & Engi, 2017). Even though most garnet grains are much smaller at 750°C (BB-253; **Fig.6** and **S6**) than at 1400°C (BB-246; **Fig.7** and **Fig.S5**), the garnet network is already well developed, which explains the high conductivity even at low temperatures (500-750°C; **Fig.10**). Garnet connectivity was reported in various natural rocks (e.g. Henjes-Kunst & Altherr, 1992; John et al., 2004; Evans et al., 2011; Vrijmoed et al., 2013; Lanari & Engi, 2017). The connectivity of garnet networks or garnet pyroxenites is documented by several studies in different geological contexts (e.g. Henjes-Kunst & Altherr, 1992; Vrijmoed et al., 2013).

4.3. Network connectivity and electrical conductivity

The interconnection of conductive phases and the topology of the conductive network control the bulk electrical conductivity of a multiphase system (e.g. Glover et al., 2000; Wang et al., 2013; Miller et al., 2015). In the system considered in this study, we have to consider two networks which themselves combine to form the bulk conductivity. The first of these networks consists of the various minerals that compose the host rock. The second is the material within the grain boundaries that contains a complex distribution of phases, which we refer to as the intergranular system.

The starting material that forms the host is a relatively homogeneous distribution of submicrometric to plurimicrometric grains of olivine, pyroxenes and accessory minerals. We used a random-distribution model to compute the bulk conductivity of the host rock based on the documented conductivity data of each phase. Although dealing with different time and space scales, the conceptualization in the present study follows the same logic as presented by Ferrand (2020). Considering a harmonic mean with arbitrary shaped and oriented volumes of conductivity σ_i and fraction X_i, a random model can be used to calculate the bulk conductivity σ^* as follows:

$$\sigma^* = \prod_{i=1}^{N} {\sigma_i}^{X_i}$$

Conductive grain-boundary impurities can significantly impact the bulk conductivity, and their influence depends on their amount and nature (Watson et al., 2010). Consequently, the conductivity within the grain-boundary network is less straightforward, as it consists of garnets, carbon and other phases distributed in a complex manner. However, when considering the effects of minor carbon impurities (**Fig.S2**), likely graphitic in the cratonic root (***section 5.2***), and given that there is no reason for carbon to be anisotropically distributed in the powder, the random model can also be used to estimate the conductivity of the carbon-bearing garnet-rich network. An alternative estimate would be to consider carbon impurities as electrical shorts between the garnet grains. The random model provides a more conservative estimate and is chosen for bulk calculations.

It should be noted that, considering that the carbon impurities are localized at grain boundaries, the carbon content of the grain-boundary conductive network is necessarily significantly larger than the bulk carbon fraction. While the bulk graphite content is estimated to be $\sim$ 0.1 wt.%, we expect, considering the intergranular system equal to 3-10% of the total volume, that the average graphite content of the grain boundaries is $<$ 10-30 vol.%. In **Fig.10** and **Fig.11**, a garnet/graphite ratio of 80:20 is assumed. Because the uncertainty about the carbon amount in both the experimental conductive network and its natural equivalent, **Fig.12** also presents simulations for ratios 70:30 and 90:10. Electrical conductivity values for given fractions of garnet and carbon are provided in **Table S3**. In the deep root of the craton, the expected form of carbon is thermodynamically stable one in mantle rocks equilibrated in reductive conditions, i.e. graphite, which electrical conductivity is not much higher than amorphous/disorganized carbon (Duba & Shankland, 1982), in comparison to silicates.

Several models exist to predict the bulk conductivity of rocks as a function of a conductive interstitial phase, typically partial melt or saline fluid (e.g. Glover et al., 2000 and references therein). Connectivity problems can be solved using the percolation theory (Gueguen & Dienes, 1989). The connectivity threshold depends on the geometry of the conductive network (e.g. Miller et al., 2015). This geometry is analogous to the melt-grain networks analyzed by Zhu et al. (2011) and Miller et al. (2015), except that instead of a homogenous melt phase (with a single conductivity value), we have a multi-phase network between grains that includes garnet and carbon as discussed above. Complementary carbon-free models have been published in a previous study to reproduce the conductivity of garnet pyroxenite channels (Ferrand, 2020).

We have compared the geometry-based models to a modified Archie's law accounting for the conductivity of both the conductive network and the silicate grains (Glover et al. 2000) **(Table S3)**. Miller et al., (2015) found that such modified Archie's law is relevant to interpret bulk conductivity values as a function of melt fraction. Using microtomography in partially molten rocks (Zhu et al., 2011; Miller et al., 2015), it was observed that the connectivity threshold strongly differs between 2-D and 3-D systems (e.g. Clerc et al., 1979), which implies that the expected connectivity level in the samples is necessarily higher than what can be observed with SEM imaging (**Fig.5** to **8**).

We have used a variety of multi-phase conductivity models shown in **Table S4** in order to cross-check the bulk conductivities measured in the laboratory. Several volume fractions were tested and preferred models correspond to the ones that reproduce the observations. As illustrated in **Fig.11**, considering a moderate garnet hydration and the presence of a minor amount of graphite, the conductive grain-boundary network is expected to represent only 1-3 vol.%. Regarding the geometry of the garnet-rich network, it appears that either the Hashin-Shtrikman upper bound, the wetted thin films or the modified

346 brick-layer models provide simulations that fit the data (**Fig.11**). Considering the uncertainty regarding
347 both the carbon fraction and the exact H content of garnet, additional simulations show that the
348 conductivity values obtained during the experiments at 3 GPa can be explained by the nucleation of
349 nanometric garnet crystals at grain boundaries. We consider the conductive network described above as
350 an experimental equivalent of larger-scale natural garnet-rich networks, such as garnet pyroxenite
351 layers/clusters that are expected in the metasomatized root of the Tanzanian craton (***section 5.1***; **Fig.S7**).

352 # 5. Extrapolation to nature and discussion

353 ## 5.1. Significance of the experimental results for the deep cratonic root.

354 Electrical models considering various connectivity modes (**Fig.10**, **Fig.11, Fig.12**) suggest that the bulk
355 conductivity of pyroxenite (e.g. BB-246; **Fig.5b**) is best reproduced by the presence of a garnet-rich grain-
356 boundary network containing scarce carbon impurities. As a consequence, we suggest that the
357 combination of a moderate H amount, the presence of iron in garnet, and the preferential distribution of
358 garnet grains and carbon impurities at the grain boundaries best explains the high electrical conductivity
359 of the pyroxenite samples at 3 GPa. This garnet-rich grain-boundary network can be seen as a laboratory-
360 scale experimental analogue of larger-scale natural garnet-rich features (Henjes-Kunst & Altherr, 1992;
361 Vrijmoed et al., 2013).

362 Garnet is ubiquitous in the deep cratonic lithosphere (> 2 GPa, i.e. > 60 km depth), but the conductive
363 anomaly is located deeper than the top of the garnet stability field (> 2.7 GPa, i.e. > 80 km depth; **Fig.4** and
364 **13a**). Furthermore, if the transition to the garnet stability field was solely the cause of the conductive
365 anomaly, such a transition should be a ubiquitous feature within cratons globally, yet that is not the case.
366 In Tanzania, the conductive anomaly corresponds to the deepest part of the cratonic lithosphere. The
367 widespread presence of garnet at these depths is consistent with previous studies that argue for increased
368 fertility with depth, associated with recent plume impingement, from which the Fe-rich dunites of the area
369 would also originate (Lee & Rudnick, 1999). As a consequence, we propose that the garnet-rich networks
370 originate from plume-induced metasomatism (***section 5.4***).

371 As illustrated in **Fig.13**, the experimental results on the pyroxenite and dunite at 3 GPa (**Fig.10b**)
372 reproduce the field conductivity values reported by Selway (2015) for the deep lithosphere of the craton
373 and the neighboring belt, respectively. We propose that the electrically conductive anomaly below the
374 craton is caused by the presence of garnet-rich network in a similar manner to the networks observed in
375 the pyroxenite samples (**Fig.13e**). The numerical models of electrical conductivity are scale-independent
376 and can apply to the thin grain-boundary networks in experimental samples and to larger garnetite or

garnet pyroxenite layers in nature. Scattered graphitic impurities, commonly introduced by plume metasomatism, may contribute to the electrical network. As previously noted (Selway, 2015), partial melting is not a plausible candidate to explain the field electrical observations, as both high shear-wave seismic velocities (O'Donnell et al., 2013) and a cool geotherm (Vauchez et al., 2005) characterize this craton. Instead, it was suggested that the conductive anomaly could be due to a H content significantly higher in the cratonic mantle than in the highly deformed Mozambique Belt (Selway, 2015). This contradicts the long-term stability of the craton and rheological studies highlighting that deformation is enhanced by the presence of water (Hirth & Kohlstedt, 2003), though differences in grain size could counter the water-induced weakening, allowing the cratonic root to remain stable (Selway, 2015).

Our results also reconcile the apparent discrepancy between MT (high conductivity) and seismic observations (fast velocities) within deep cratonic roots at 70 ±10 km depth (O'Donnell et al., 2013). The volume fraction of garnets required for the electrical model are not so substantial that a significant impact on bulk seismic velocity should be expected. It should be noted, however, that an enigmatic seismic discontinuity was evidenced beneath North America around these depths (Hales, 1969). Both the results and simulations (**Fig.10** to **12**) recall that the connectivity of conductive minerals is the main parameter controlling bulk electrical conductivity, rather than their actual volume fraction. Hence, the garnet fraction needed to explain the electrical structure is sufficiently small that a commensurate change in seismic velocities is not expected (James et al., 2003). Although the distribution of garnet-rich networks within the deep Tanzanian lithosphere is unknown, occurrences of garnet interconnected over long distances are observed in nature. In our samples, the conductive network contains minor amounts of carbon. The root of the craton is reported as the source of carbon enrichment (Muirhead et al., 2020). Garnet networks, reported both in xenoliths (**Fig.S7**; Henjes-Kunst & Altherr, 1992) and outcrops (Vrijmoed et al., 2013), can be caused by mantle fertilization.

Although conductive lithospheric mantle is not ubiquitous in cratons, there are examples of elevated lithospheric conductivity, including the rifted Yilgarn craton, Australia (Wang et al., 2014) and the Dharwar craton near the Deccan traps, India (Patro & Sarma, 2009). The North China craton is thought to have been disrupted by plume impingement (Wang et al., 2015) and has a signature that reflects thinner lithosphere after delamination (Ye et al., 2018). Metasomatism due to plume impingement has been suggested as a potential cause of the destruction of cratons (Foley, 2008; Wang et al., 2015; Celli et al., 2020). Elevated conductivities suggest extensive metasomatism by the African superplume, a model supported by numerical modelling for the East African rift system in the area (e.g. Koptev et al., 2016). Thus, the MT

model of Tanzania (Selway et al., 2015) could present an image of lithosphere primed to break away. Root delamination would eventually erase the conductive anomaly.

5.2. Type and amount of carbon present & oxygen fugacity

Northern Tanzania is volcanically active – a prime example is Mt. Kilimanjaro – and the lithospheric mantle of the region is known to be CO_2-rich, as revealed by various xenoliths containing either carbonates (e.g. Lee & Rudnick, 1999) or carbonatite metasomatism (Rudnick et al., 1993). Xenoliths of the Lashaine area contain about 3 wt.%. of H_2O and 1.4 wt.% of CO_2 (Dawson et al., 1970), which suggests that the lithospheric mantle contains 10-100 ppm of CO_2 on average. This is further confirmed by a recent work in the studied area (Halldórsson et al., 2022), reporting high CO_2 contents between 0.6 to $1.7x10^{-6}$ cm^3/g in pyroxenite xenoliths. At high pressure (> 1 GPa) in the mantle, reductive conditions should favor graphitic carbon impurities at grain boundaries, which can be easily identified and speciated using Raman spectrometry (e.g. Pearson et al., 1994). Yet, Raman spectrometry reveals limited crystallinity (**Fig.S2**), as explained in details in the literature (e.g. Deldicque et al., 2023). The relatively cold geotherm of the craton induces kinetics issues within the studied xenoliths that maintain the carbon in a less mature state (**Fig.S2**), expected almost as conductive (Duba & Shankland, 1982; Watson, 1986); in contrast, the deep root should host graphitic carbon at grain boundaries due at intermediate temperatures.

The preservation of the rhenium furnace, along with the stability of minor grains of Th-Ta-Ni alloy and the presence of titanium phosphide (**Fig.S5** and supplementary text) indicate a reducing environment, as expected in the cratonic mantle at 3 GPa ($\log fO_2$ = -2; ΔFMQ; Frost & McCammon, 2008). In such reduced conditions at elevated temperatures, carbon is more likely in the form of graphite that immobilizes at grain boundaries (Watson, 1986). This confirms that the studied xenoliths originate from relatively shallow depths, consistently with the absence of garnet in the starting material. In contrast, higher temperatures in the root of the craton would favor graphitization of such organic matter. It should be noted that the term 'graphitic carbon' is often used as a general description of carbon in conductivity studies, because carbon crystallinity is a minor parameter compared to its connectivity.

Both the nature and repartition of the carbon impurities should be considered to evaluate the impact of carbon on electrical conductivity (Wang et al., 2013). A previous study determined a percolation threshold of graphite GB impurities of ~ 1 wt.% (Wang et al., 2013), while lower graphite contents (~ 0.1 wt.%) are associated with relatively low bulk conductivities (Watson et al., 2010). In the model, we assume the carbon content ~ 0.1 wt.% based on Raman spectrometry (**Fig.S2**) and consistently with regional constraints (Dawson et al., 1970; Chin, 2018; **Table 1**), and evidence the nucleation of nano- to microgarnet at grain boundaries, likely involving carbon impurities in the conductive network (**Fig.11**, **Fig.12**).

In addition, carbon solubility in olivine is relatively low compared to pyroxenes and garnet, but increases with pressure (Keppler et al., 2003). As ENG8 consists of 95% olivine, it is possible that the observed drop in conductivity with increasing pressure is due to the effect of pressure as well as enhanced carbon solubility.

5.3. Remarks on the electromagnetic profile

Although the focus of the present study is the root of the Tanzanian craton, the MT profile (Selway (2015) shown in **Fig.13** presents other high-conductivity anomalies, localized at shallow depths (≤ 35 km depth; ≈ 1.1 GPa) in magmatic areas. These anomalies require other explanations, such as melt networks or hydrothermal fields. Such melt networks may correspond to the mature rift system of the Central Vallee, Ethiopia, where near-surface high conductivity (∼1 $S.m^{-1}$) is demonstrably related to magmatic activity (Keir et al., 2009). This is also the case for the Eyasi rift and Kilimanjaro regions at similar depths (**Fig.13**), where connected networks of volatile-bearing basaltic melts well explain (**Fig.10b**) shallow high-conductivity anomalies (≥ 10^{-1} $S.m^{-1}$; ≤ 1 GPa; Selway, 2015).

Importantly, it should be noted that the MT data are unable to resolve whether the anomaly crosses the Lithosphere-Asthenosphere Boundary (LAB). The MT profile reinterpreted in this study in light of our experimental results has limitations inherent to either the geological context or the geophysical method. The entire lower portions of the lithospheric mantle of the Tanzanian craton appear as a uniform conductor in the inversion model presented by Selway (2015). It is not possible to identify the lower electrical bound of the conductivity anomaly. If graphite acts as an important connector of the garnet grains, we would expect this mechanism to switch off upon the transition from the graphite to the diamond stability zone at a depth of ∼ 150 km, or most certainly at a depth above the LAB (**Fig.13**).

5.4. Plume impingement and evolution of the cratonic lithosphere

Zones with thin lithosphere are known to act as sinks for a buoyant mantle plume (e.g. Sleep, 1997). In particular, numerical modelling of plume-lithosphere interactions in the East African rift system shows that the mantle plume is deflected by the thick root of the Tanzanian craton and is preferentially channeled towards the neighboring mobile belt (Mozambique Belt), characterized by a thinner lithosphere (e.g. Koptev et al., 2016). Spatial variations in the lithospheric geotherm associated with plume impingement would induce lithospheric deformations around the craton (Koptev et al., 2018). However, our results, together with other recent studies (e.g. Muirhead et al., 2020) highlight deep metasomatism of the Tanzanian craton, which would mean that the lateral flow near the LAB is not incompatible with a significant incorporation of plume elements towards the deep cratonic lithosphere.

Although fertilization processes may depend on geological settings and would not necessarily require the action of a mantle plume (Griffin et al., 2009; O'Reilly & Griffin, 2013), we would favor the plume impingement interpretation in the context of the East African Rift. The increase of the fraction of garnet pyroxenites within the cratonic root would induce an increase in density, which could contribute in lithospheric delamination (e.g. Foley, 2008; Ye et al., 2018; Hu et al., 2018; Celli et al., 2020). Furthermore, lithospheric delamination can open asthenospheric windows responsible for delamination-induced magmatism (Kay & Kay, 1993), prone to act as positive feedback for root metasomatism and associated densification.

It is likely that garnet pyroxenites exist in the deep lithospheric mantle of both the Tanzanian Craton and Mozambique Belt, as illustrated on **Fig.13**, but these garnet pyroxenites need to be connected to significantly impact the electrical conductivity. Considering an iterative interaction for millions of years between plume-derived melts/fluids and rocks of the cratonic root and a lateral percolation flow towards the Mozambique Belt, the formation of well interconnected high-conductivity pathways is more likely within the cratonic root. We propose that the observed electrical anomaly could be the signature of a critical state of a cratonic root between stability and disruption.

Conclusions

Electrical conductivity measurements at high pressures and temperatures on dunite and pyroxenite xenoliths from Tanzania allow reproducing the high conductivity anomaly of the deep Tanzanian Craton. High electrical conductivity values are associated with connected networks of garnet-rich rocks, with natural H contents limited to values < 0.1 vol.%. The experiments indicate that the conductive rocks most likely consist of garnet pyroxenites, in which both garnet and pyroxenes can bear significant H amounts.

Once garnet becomes stable in fertile mantle rocks (> 60 km, 1.7 GPa), it can nucleate at grain boundaries (e.g. this study; Henjes-Kunst & Altherr, 1992) or as connected reaction rims (e.g. Vrijmoed et al., 2013), forming the backbone of a conductive network. At 3 GPa, such garnet-rich networks increase conductivity by a factor of 100 regardless of temperature. Numerical models show that the observed low ($< 10^{-2}$ Sm^{-1}) and high ($> 10^{-1}$ Sm^{-1}) conductivity values are best explained by low and high degrees of garnet connectivity, respectively. Such high electrical conductivities in cratonic roots can be explained by the presence of connected garnet clusters or garnet pyroxenites, suggesting mantle fertilization.

In all likelihood, the high electrical conductivity in the root of the Tanzanian Craton highlights current plume impingement that has lasted for millions of years, consistently with the up-to-date knowledge on the area. Deep melts/fluids would have iteratively percolated and fossilized, progressively increasing the

amount and connectivity of electrically conductive rocks within the deep lithosphere. Although our results are consistent with long-term craton stability, the garnet-rich network likely results from continuous metasomatism due to plume impingement and might represent an unstable structure prior to loss of cratonic lithosphere.

Acknowledgments

We thank Rong Zhang and Danielle Shields for assistance in the laboratory, Rob Evans (WHOI) for key discussions on magnetotellurics, Christian Chopin for the constructive discussion on mineral identification and stability conditions, Xin Zhong and Damien Deldicque for key advices and explanations about Raman data acquisition and interpretation, and Timm John for providing key references about garnet connectivity in natural rocks. This work is partly funded by the *Alexander von Humboldt* Foundation and the Labex *VOLTAIRE* (Université d'Orléans). We acknowledge SIO-PEPL for the facility and Kurt Leinenweber for providing cell assemblies; use of the COMPRES Cell Assembly Project was supported by COMPRES under NSF Cooperative Agreement EAR 1661511. TPF thanks Jonathan Souders (UCSD – SiO IGPP) for the technical expertise on electrical circuits, Sabine Faulhaber (UCSD Nanoengineering Dept.) for her help with scanning electron microscopy, Isabel Rivera-Collazo (UCSD Anthropology Dept.– SIO) for her help with the particle size analyzer and Sean Curran (UCSD – SiO GRD) for his help with pixel counting (garnet fraction estimate).

Authors contributions

EJC provided the xenoliths powders, analyzed their mineralogy and performed the SIMS measurements. TPF performed the experiments, collected the electrical data, microstructural observations and Raman data and prepared the figures. The authors discussed the results, draw interpretations and perspectives and wrote the paper.

Tables

Table 1: Compositions (XRF) of the Tanzanian and Chinese rocks on which electrical data exist.

Location	Northern Tanzania					China		
	Engorora			Lashaine		Dengpa, Tibet	Wanquan, HeBei	
Sampling	Xenoliths			Xenoliths		Outcrop	Xenoliths	
Nature	Dunite ENG-8	Pyroxenite ENG-7	Host lava	Lherzolite	Host lava	Dunite	Lherzolite	Pyroxenite
Major elements oxides (wt.%)								
SiO_2	39.94	51.40	43.09	44.37	39.44	41.36	44.79	48.08
TiO_2	0.16	0.57	2.47	0.08	2.37	0.01	0.08	0.62
Al_2O_3	0.35	2.87	5.71	2.44	5.84	0.12	2.31	6.25
Cr_2O_3	0.12	0.37	0.39	0.48	0.11	*n.d.*	*n.d.*	*n.d.*
FeO_T	13.56	8.82	11.56	7.27	12.88	3.86	8.14	9.24
Fe_2O_3	*n.d.*	*n.d.*	*n.d.*	0.85	9.21	0.34	1.89	3.04
FeO	*n.d.*	*n.d.*	*n.d.*	6.42	4.59	3.52	6.25	6.20
MnO	0.19	0.18	0.20	0.09	0.17	0.04	0.13	0.15
MgO	43.87	17.66	18.71	42.14	17.67	52.34	40.72	17.27
CaO	0.91	17.09	12.35	1.45	12.24	0.95	2.26	15.43
Na_2O	0.00	0.51	1.24	0. 25	1.97	0.01	0.07	0.56
K_2O	0.03	0.06	0.75	0.08	0.99	0.02	0.02	0.02
P_2O_5	0.24	0.17	0.51	0.05	0.81	0.01	0.01	0.02
H_2O^+	*n.d.*	*n.d.*	0.74	0.39	0.8	0.46	1.28	1.58
H_2O^-	*n.d.*	*n.d.*	*n.d.*	0.18	2.26	*n.d.*	*n.d.*	*n.d.*
CO_2	*n.d.*	*n.d.*	0.74	0.25	1.41	0.08	0.13	0.21
Total	99.38	99.69	96.98	99.52	99.88	98.72	98.53	97.64
Mg#	0.85	0.78	0.74	0.85	0.71	0.961	0.899	0.455
Ref.	Chin, 2018			Dawson et al., 1970		Wang et al., 2008		

528 **Table 2: Composition and H content of the Engorora xenoliths.**

	Modal mineralogy cpx:opx:ol:chr	Average cpx H (ppm H_2O)	1σ*	Average opx H (ppm H_2O)	1σ*	Average olivine H (ppm H_2O)	1σ*	Whole-rock Mg#	Whole-rock reconstructed (ppm H_2O)
ENG14**	14:tr:85:1	64	22	not present	n/a	16	(1 grain)	84	22
ENG12	46:tr:52:2	124	42	not present	n/a	35	(1 grain)	82	75
ENG7	87:11:2:tr	273	62	163	50	not analysed	n/a	78	255

cpx = clinopyroxene, opx = orthopyroxene, ol = olivine, chr = chromite, tr = trace;
*1σ is the standard deviation of all spot measurements per xenolith;
**ENG14 is petrologically and texturally very similar to ENG8 (dunite used in this study).

529 Modal mineralogies were calculated by least-squares inversion of the whole-rock and average mineral major
530 element compositions. For details on water content determination using secondary ion mass spectrometry
531 (SIMS), see the ***Supplementary Information*** (***section 1.3***)**.** It should be noted that Raman spectrometry identifies
532 a H amount in ENG8 larger than ENG7, which suggests that H in ENG8 (and most probably ENG14) would be
533 preferentially localized at grain boundaries or tiny grains whereas SIMS measurements are performed on grain
534 interiors (spot = 8 µm).
535

536 **Table 3: Summary of the experiments.**

Run	Starting material	P (GPa)	T_{max} (°C)	Hydrogen	carbon	Microstructural observations
BB-244	ENG7: pyroxenite xenolith powder	1.5	1403	~200 ppm H_2O	10-100 ppm CO_2; < 0.1 wt.% graphite	(sub)micrometric spinel crystals localized in melt pockets.
BB-253		3.0	750			Submicrometric garnets at grain boundaries; no melting.
BB-246			1400			(sub)micrometric garnet networks.
BB-254			1575			crystallized melt pockets containing Fe-rich dendrites (melting of the electrodes).
BB-238	ENG8: dunite xenolith powder	1.5	1342	~25 ppm H_2O		melt wetting triple junctions.
BB-247		3.0	1449			some garnet grains, not connected; few quenched silicate melt pockets.

537 The H contents come from SIMS measurements on olivine and pyroxene crystals from the studied xenoliths,
538 presented in the ***Supplementary Information*****.** For detailed microstructural observations, see **Fig.5-9**.

Figures

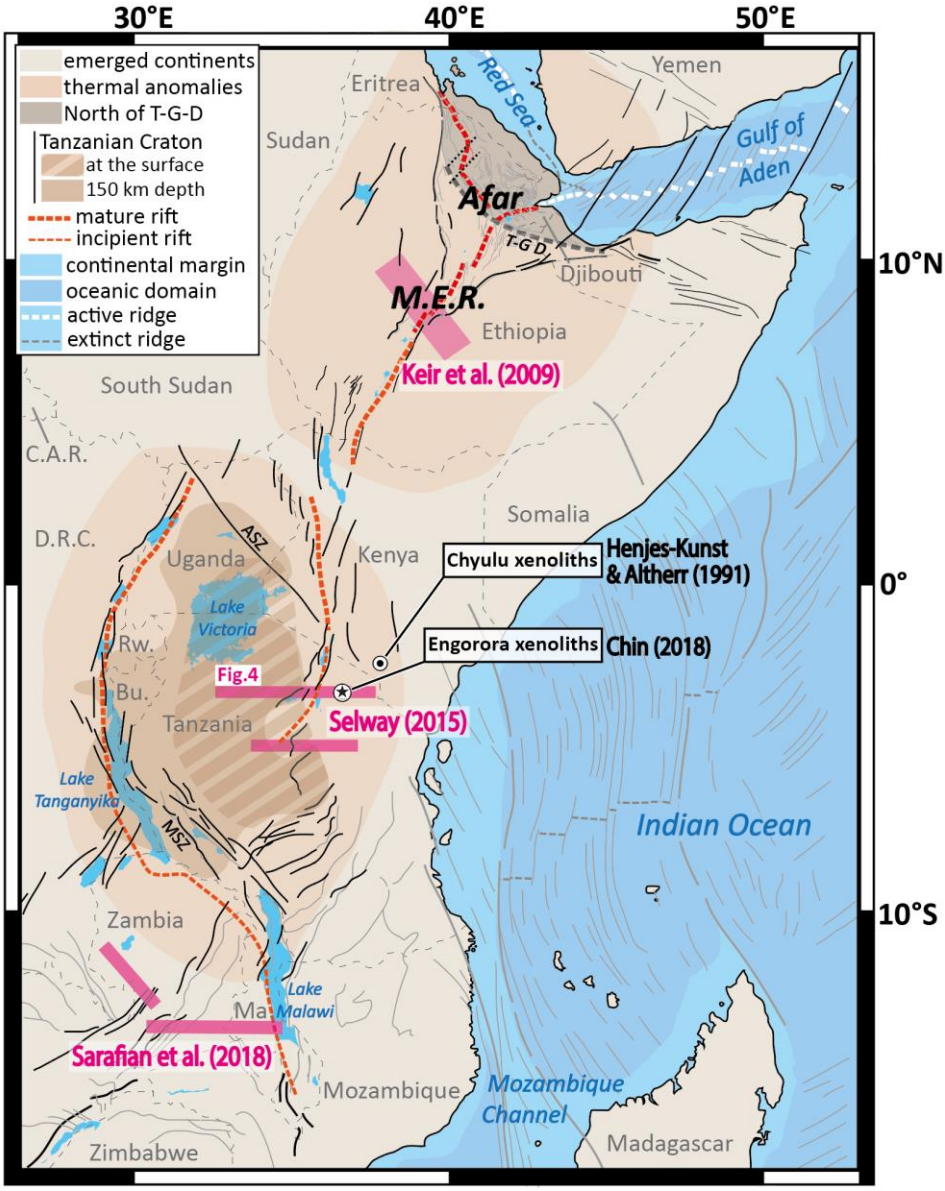

Figure 1: Synthetic map of the East African Rift, adapted from Chorowicz (2005), Sarafian et al. (2018) and Lemna et al. (2019), with oceanic fabric from Phethean et al. (2016). The limits of the Tanzanian Craton are from Koptev et al. (2016). The Blackstar indicates the origin of the Engorora xenoliths (Chin, 2018) used as starting material in this study; the black dot locates the origin of the Chyulu xenoliths (Henjes-Kunst & Altherr, 1992). Pink segments locate the profiles of previous magnetotelluric studies across the Tanzanian (Selway, 2015) and Zambian (Sarafian et al., 2018) incipient rifts, and across the Main Ethiopan Rift (M.E.R.; Keir et al., 2009). Legend: ASZ: Aswa Shear Zone; MFZ: Mughese Fracture Zone; T.G.D. = Tendaho-Goba'ad Discontinuity. Countries abbrv.: Bu. = Burundi; C.A.R. = Central African Republic; D.R.C. = Democratic Republic of the Congo; Ma. = Malawi; Rw. = Rwanda.

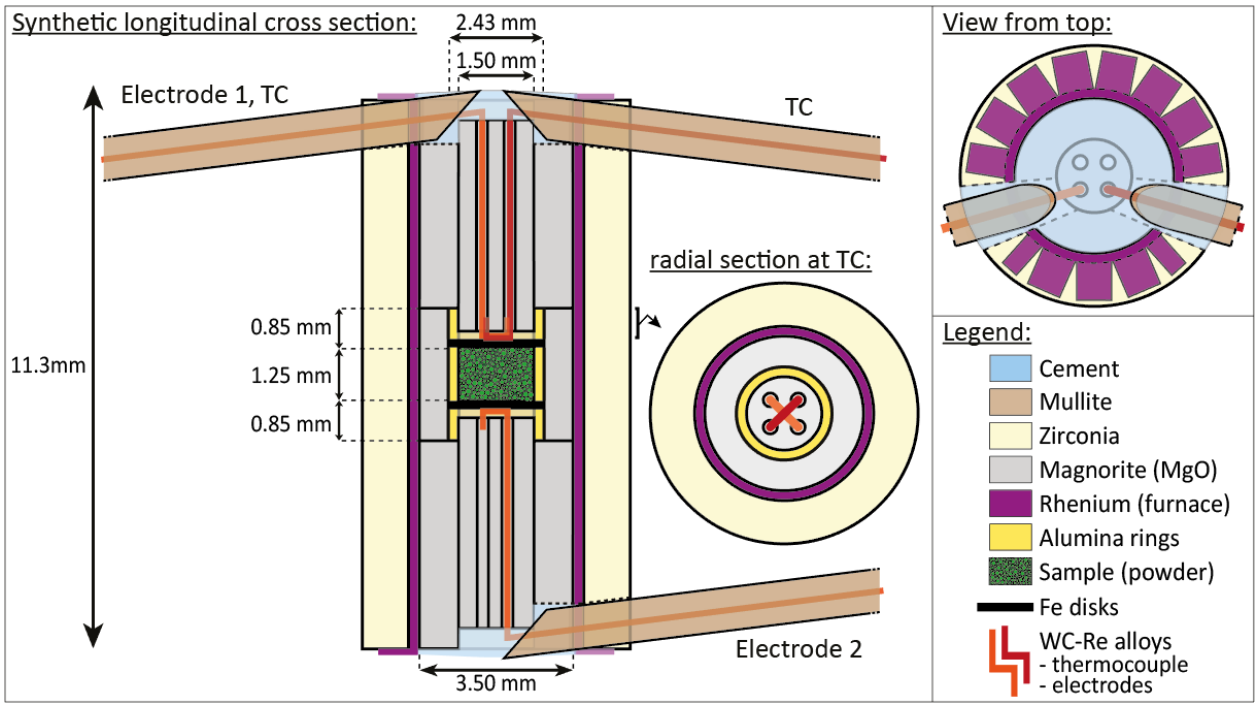

Figure 2: Experimental assembly. Synthetic sketch of the 14/8 COMPRES electrical assembly. Experiment BB-238 was performed using a 4-electrodes assembly (4 wires), which consist of a "symmetrical" assembly with 2 thermocouples.

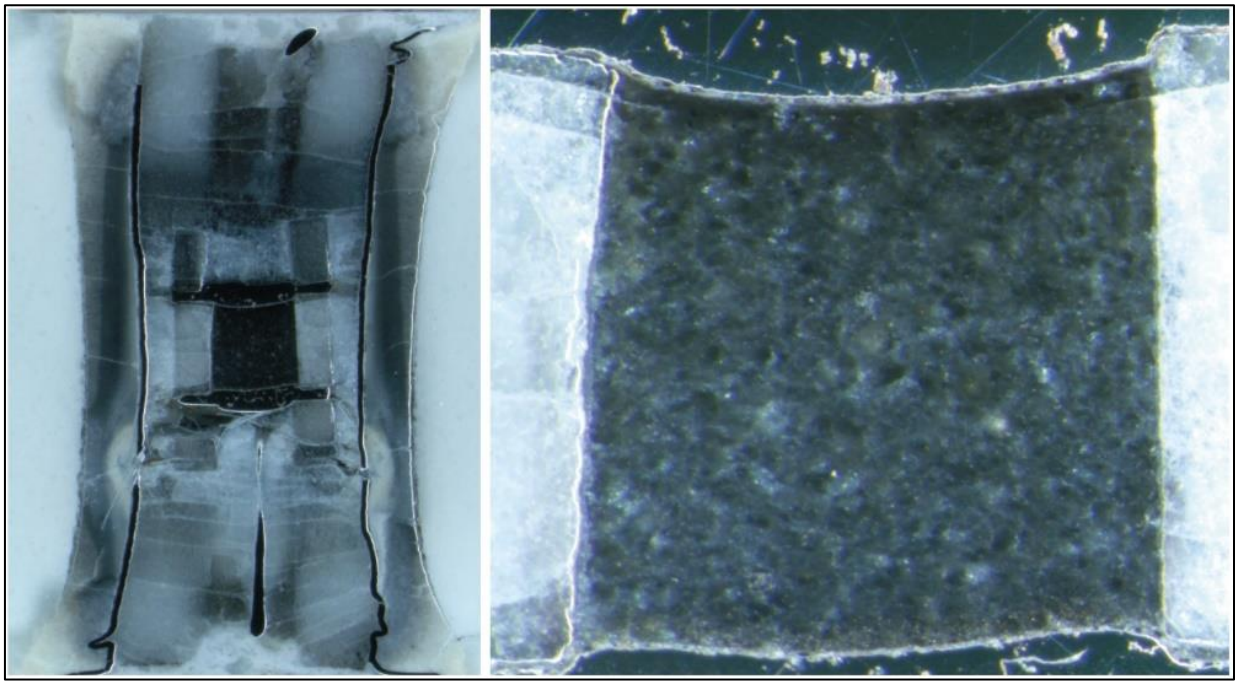

Figure 3: Recovered assembly. Run BB-246 (see Table 3): clinopyroxenite ENG7 pressurized to 3 GPa at temperatures up to 1400 ^{o}C. Microstructural observations are shown in **Fig.5b** and **Fig.7**. Electrical data are given in **Fig.10**.

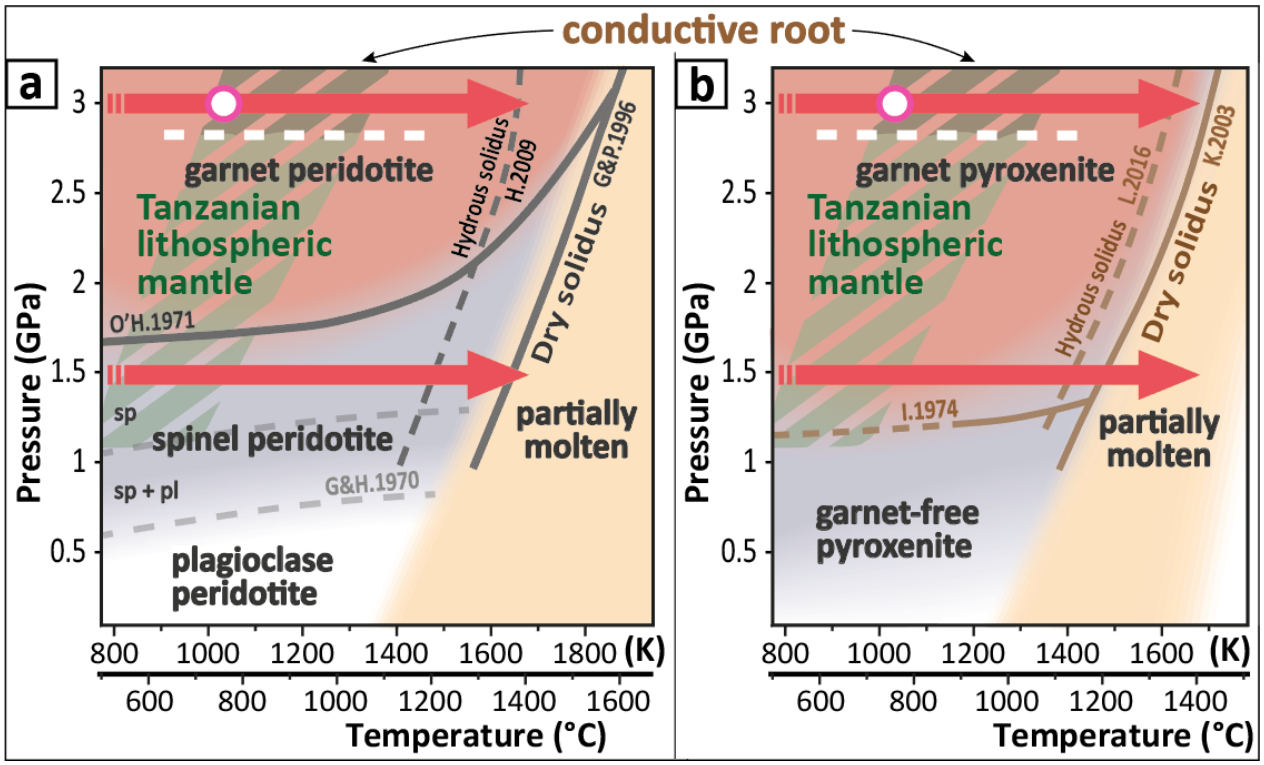

Figure 4: Experimental conditions and paragenesis expected from thermodynamics. Pressure-temperature diagram summarizing experimental conditions (red arrows) and highlighting the garnet stability field in mantle rocks (**a** = peridotites; **b** = pyroxenites) and the Tanzanian lithospheric mantle. The white dot indicates the maximum temperature (750°C) during experiment BB-253 (ENG7, 3 GPa; no elec. data). The white dashed line indicates the minimum pressure expected at ≈ 100 km depth (i.e. top of the conductive anomaly = craton root) Legend: pl = plagioclase; sp = spinel. Ref: G&P.1996 = Gudfinnsson & Presnall (1996); H2009: Hirschmann et al. (2009); I.1974 = Irving (1974); K.2003 = Kogiso et al. (2003); L.2016: Lambart et al. (2016); O'H.1971 = O'Hara et al. (1971); G&H.1970 = Green & Hibberson (1970).

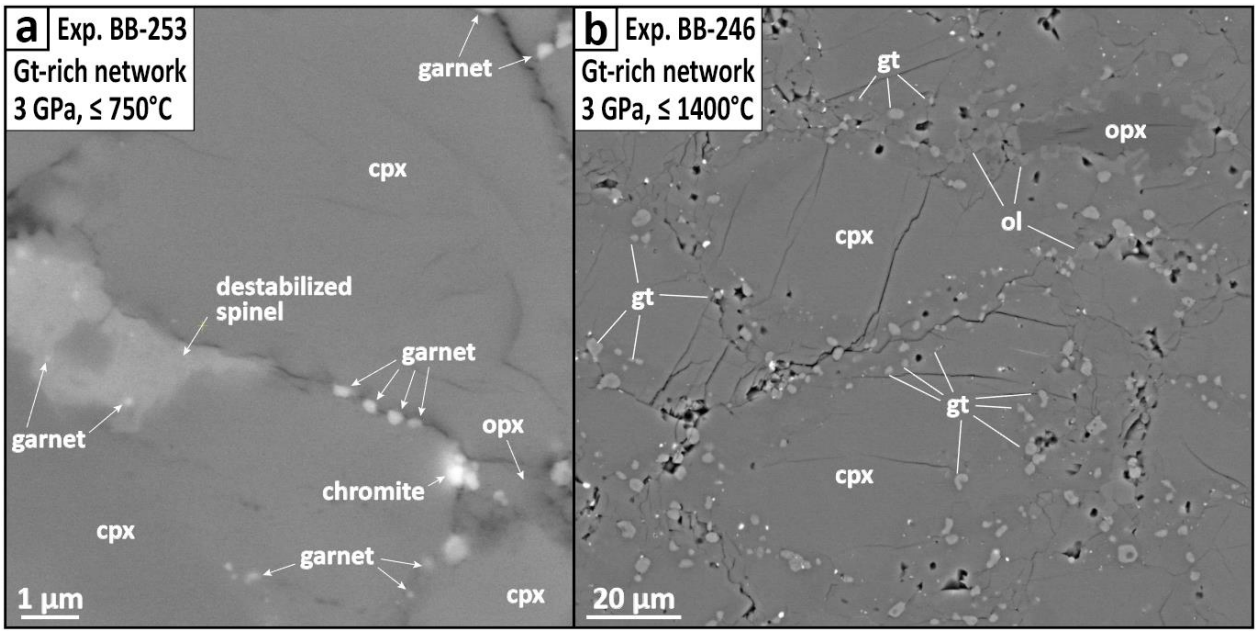

Figure 5: High conductivity due to hydrous Fe-rich garnet networks at high-pressure. a: Backscattered electron image (BSE) of an experimental garnet network (3 GPa, quench at 750°C), showing a destabilized spinel and submicrometric garnets crystallizing along grain boundaries; **b:** High-temperature garnet-rich channels (3 GPa, quench at 1400°C), showing larger garnet grains due to enhanced diffusion. For additional BSE images, see **Fig.6** to **9**. For EDS mapping, see **Fig.S5** and **S6**. During the spinel-garnet transition, Fe diffuses from destabilized spinel and oxides, while Al, Ca and OH are consumed from the surrounding minerals. Abbrev.: cpx = clinopyroxene; gt: garnet; ol = olivine; opx = orthopyroxene.

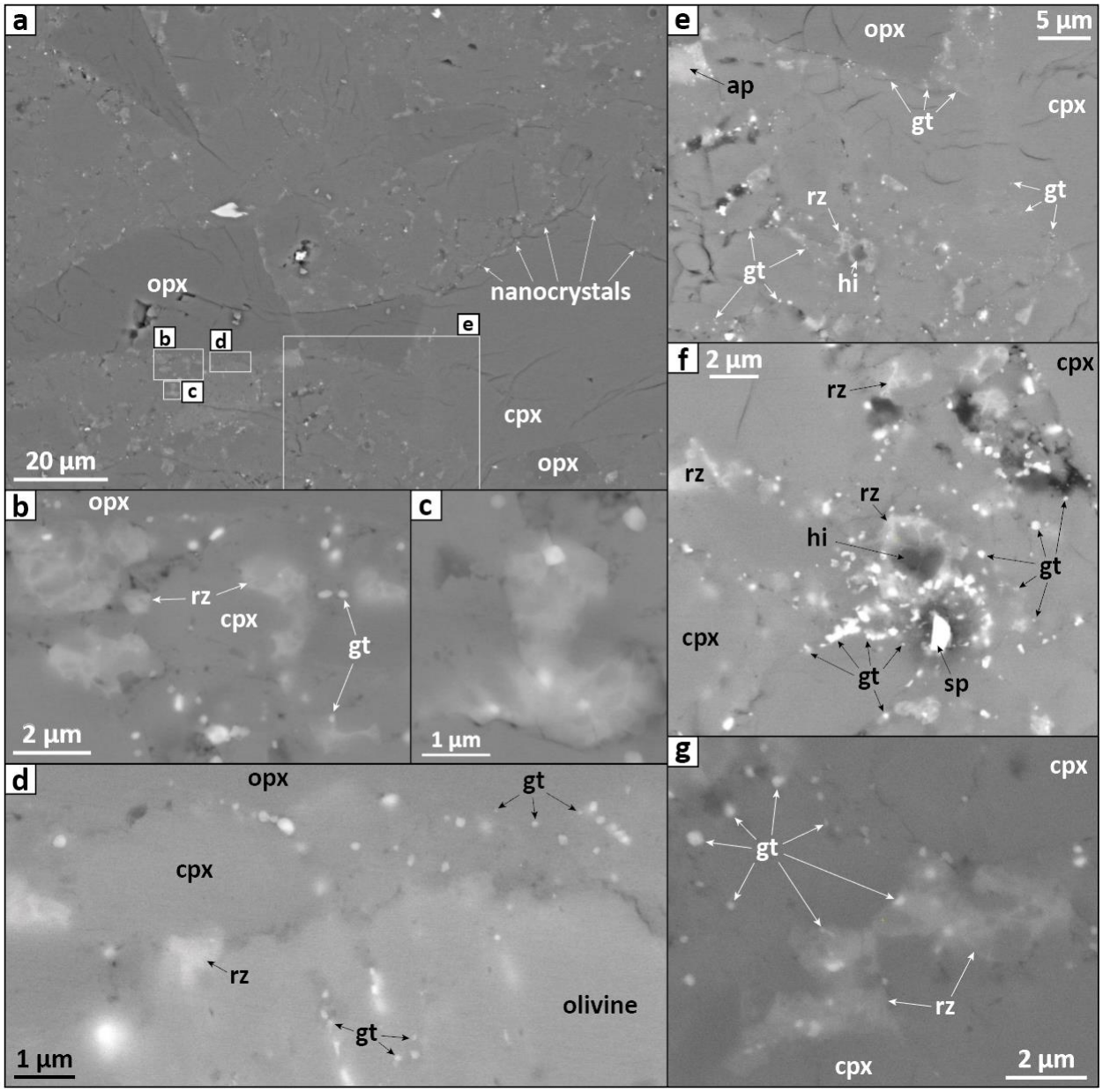

576

577 **Figure 6: Additional BSE images on sample BB-253 (pyroxenite, 3 GPa, 750°C).** Supplement of **Fig.5a**.

578 Abbrev.: cpx = clinopyroxene; gt: garnet; hi = hibonite; opx = orthopyroxene; rz = reaction zone; sp = spinel.

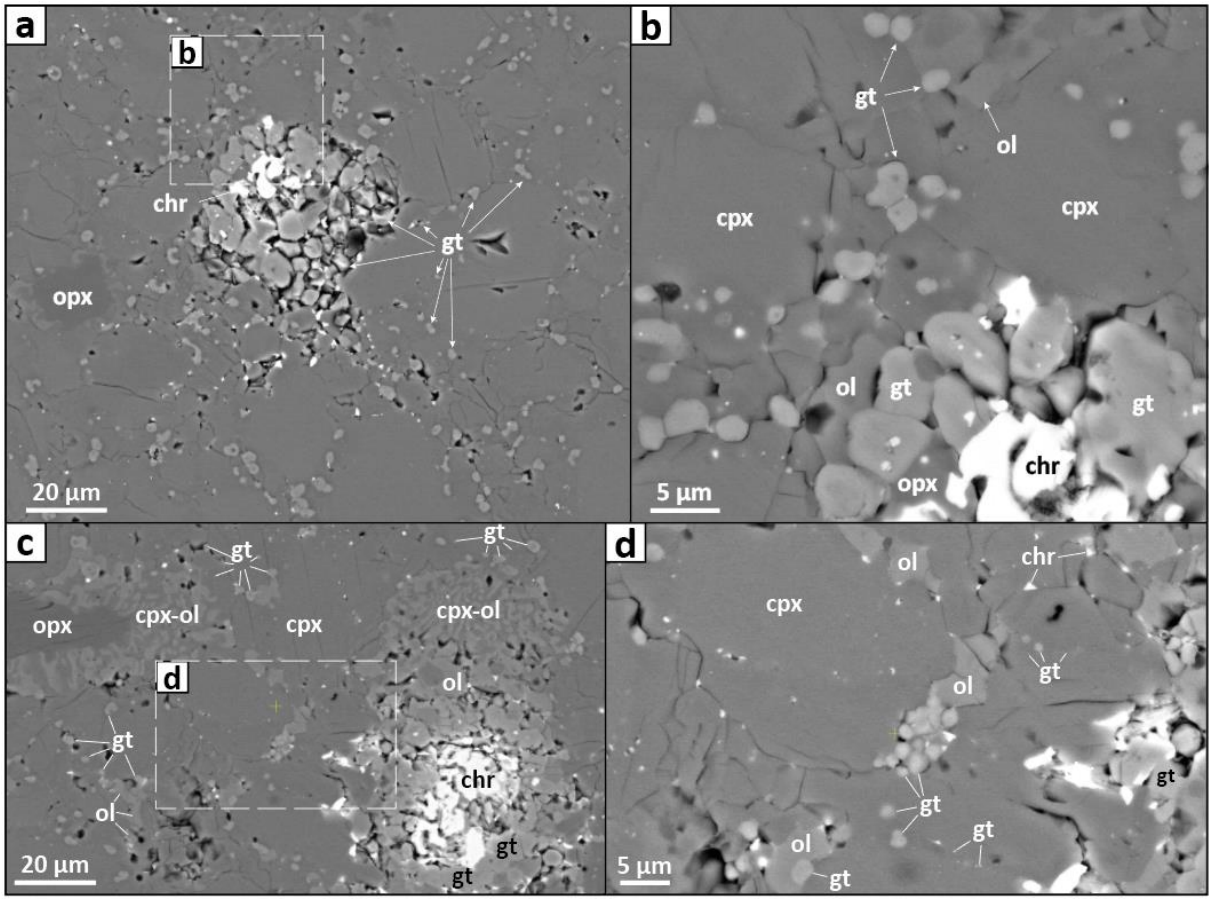

Figure 7: Additional BSE images on sample BB-246 (pyroxenite, 3 GPa, 1400°C). Supplement of **Fig.5b**. Networks of micrometric garnet crystals develop along grain boundaries throughout the sample. Larger garnet grains grow at the expense of Al-rich spinel, while chromite crystals remain stable. In addition, symplectites develop between opx, cpx and accessory minerals, which highlight metamorphic reactions. Abbrev.: chr: chromite; cpx = clinopyroxene; ol = olivine; opx = orthopyroxene; gt = garnet.

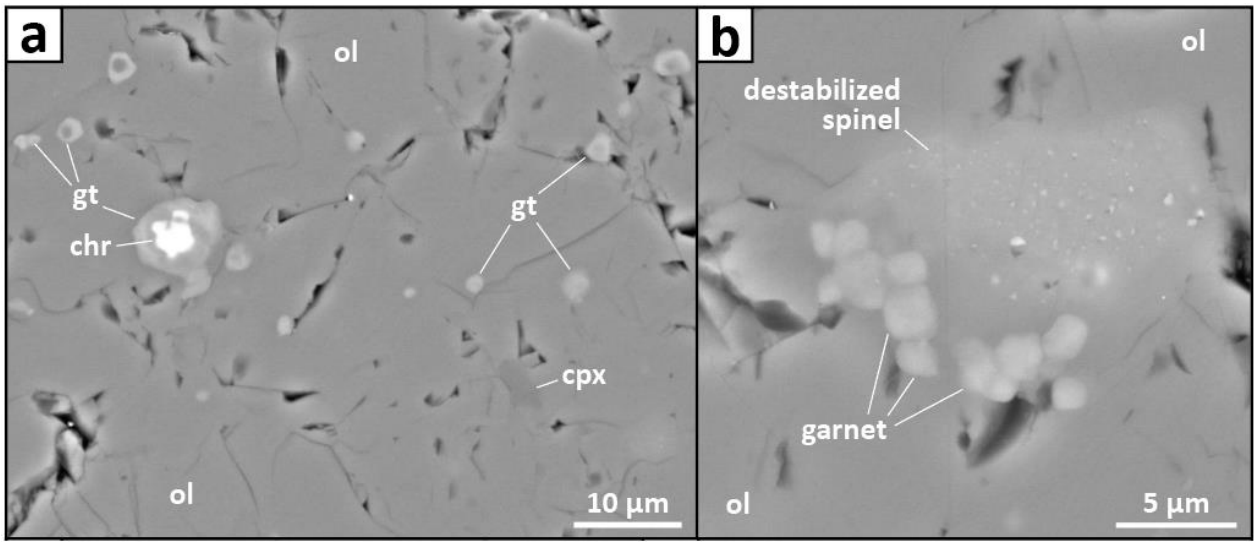

Figure 8: Additional BSE images on sample BB-247 (dunite, 3 GPa, 1449°C). Micrometric garnet grains grow only locally, in the vicinity of minor metal oxides (**a**) and destabilized spinel (**b**). Abbrev.: cpx = clinopyroxene; ol = olivine; chr: chromite; gt = garnet.

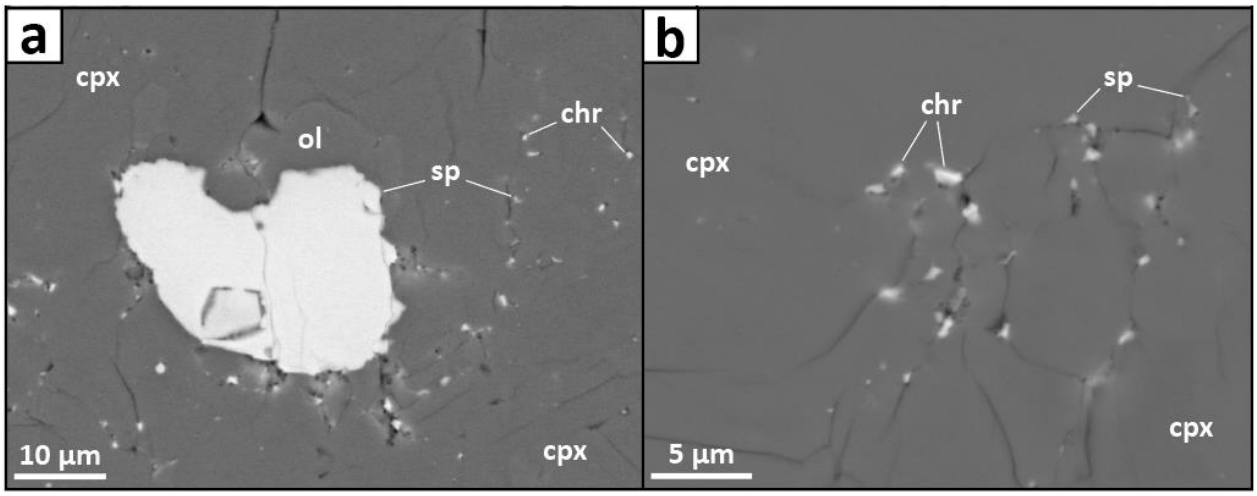

Figure 9: Additional BSE images on sample BB-244 (pyroxenite, 1.5 GPa, 1403°C). No garnet is observed. Both chromite and Al-rich spinel, originating from the xenolith powder, remain stable. Abbrev.: ol = olivine; cpx = clinopyroxene; chr: chromite; sp = spinel.

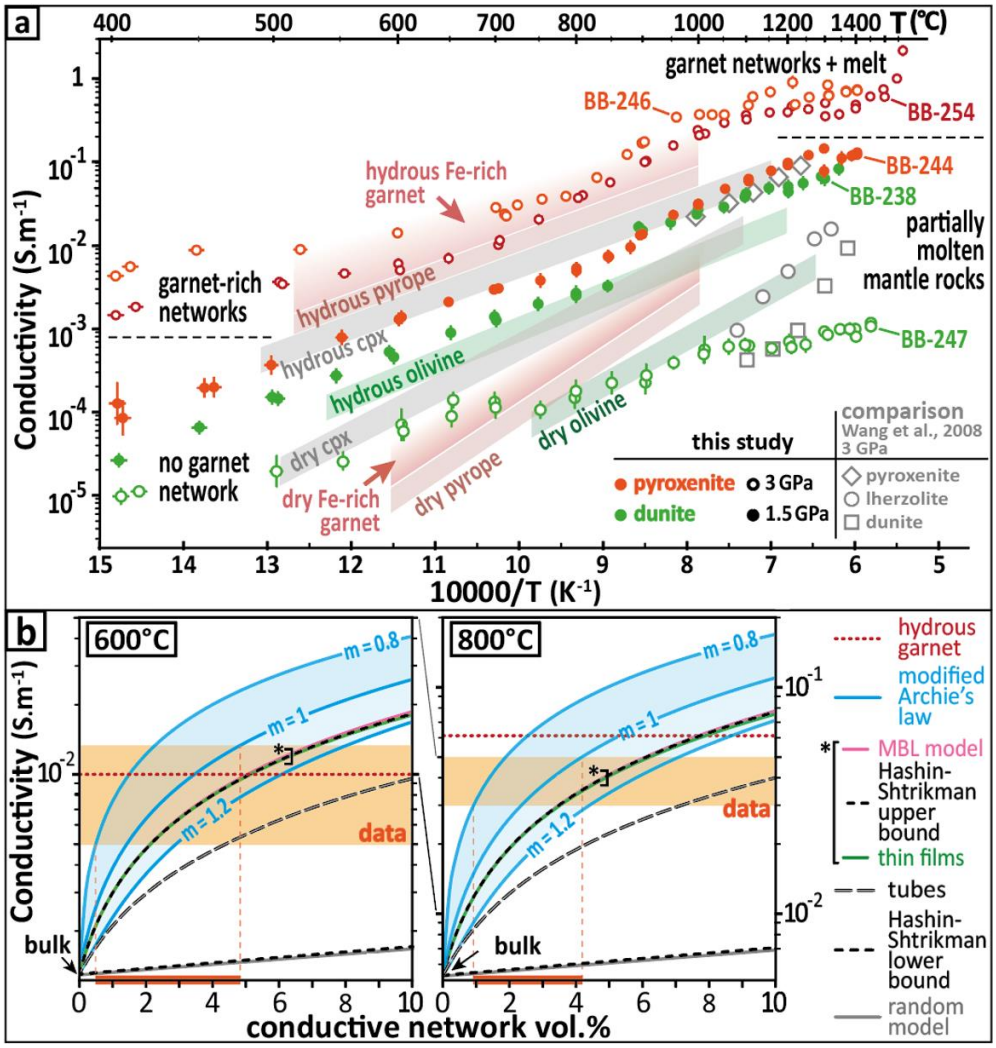

Figure 10: Experimental results and comparison with models. (a) Electrical conductivity versus reciprocal temperature for the Engorora xenoliths, at 1.5 GPa (solid circles) and 3 GPa (open circles). For comparison, the green, grey and red shades correspond to electrical conductivity values for dry (X_{Fe} = 0.1, 6-19 GPa; Yoshino et al., 2012) and hydrous olivine (465 ppm H_2O; Gardés et al., 2014), dry and hydrous (375 ppm H_2O) clinopyroxene (Yang et al., 2011) and dry pyrope (Py_{73}-Alm_{14}-Grs_{13}, 3 GPa; Dai et al., 2012) and hydrous pyrope (465 ppm H_2O; 3 GPa; Dai et al., 2012). **(b)** Conductivity simulations based on several models and compared to the experimental data at 600 and 800°C, i.e. before any melting. Grain-boundary network: 80:20 garnet/graphite circuit (~0.1 wt.% carbon). The orange box indicates the experimental electrical data at a given temperature (uncertainty range) extracted from **Fig.10a**, for comparison with the models (listed on the right side). The thick red line on x axis is the volume fraction of connected conductive network as deduced/extrapolated from the comparison between the electrical data and the connectivity models. For details on the models, see the ***SI***. For additional simulations, see **Fig.11** and **Fig.12**. The even higher conductivity observed in this study is attributed to hydrogarnet-rich Fe-rich pyrope. A summary of experimental conditions and results is provided in **Fig.4** and **Table 3**, including experiment BB-253 (ENG7,

P = 3 GPa, T ≤ 750°C), for which no electrical data was recorded. The parameters and different models are provided in **Table S3** to **Table S4**.

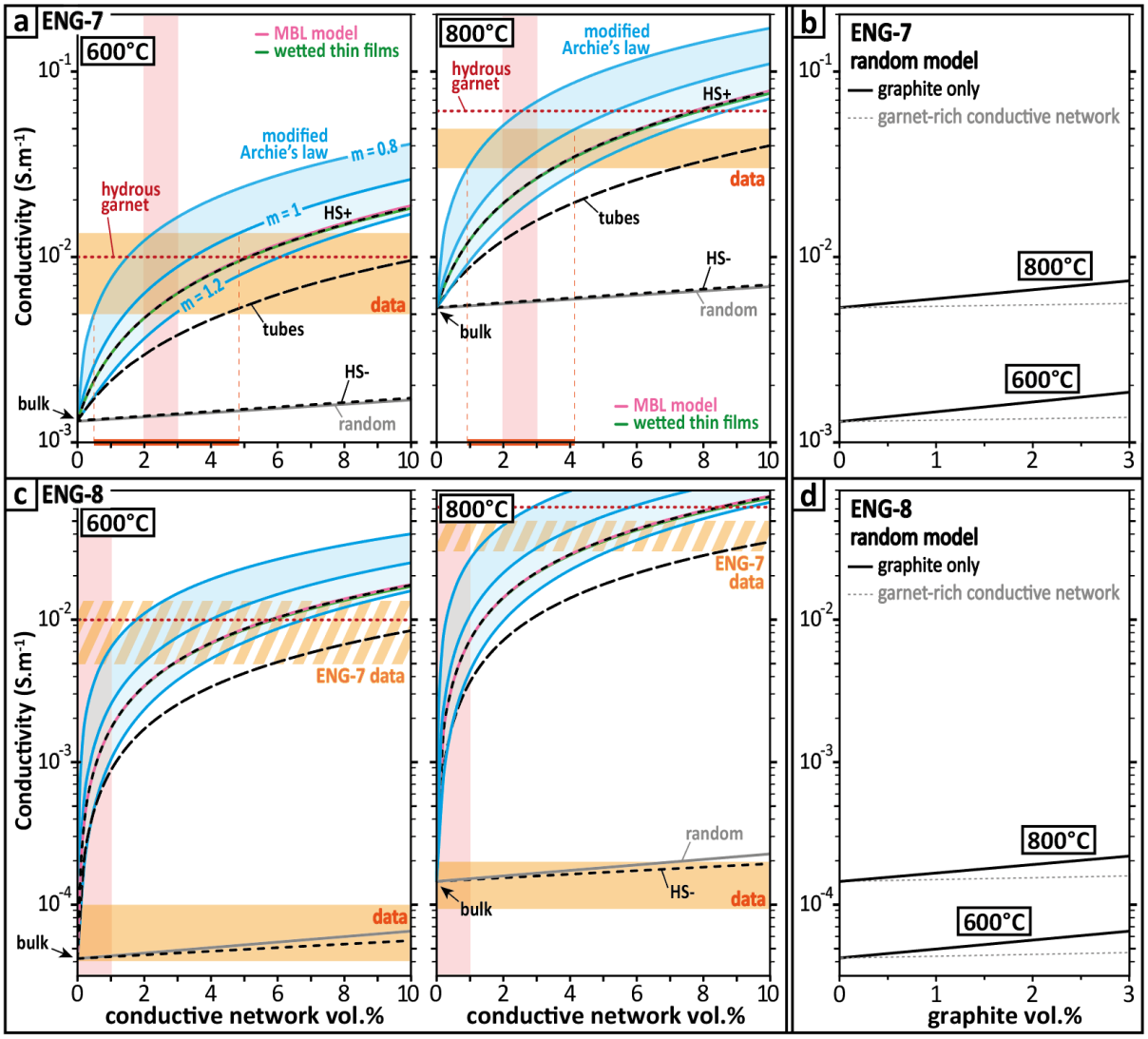

Figure 11: Conductivity simulations considering various geometries. Calculations for ENG7 (**a-b**) and ENG8 (**c-d**) at 600 and 800°C (no partial melting involved). The parameters considered for the models are listed in **Table S3**, and the formula are detailed in **Table S4.** Here the H amount in garnet is assumed to be 465 ppm. See **Fig.S6** for other H amounts. A table of values is provided in **Table S5**.

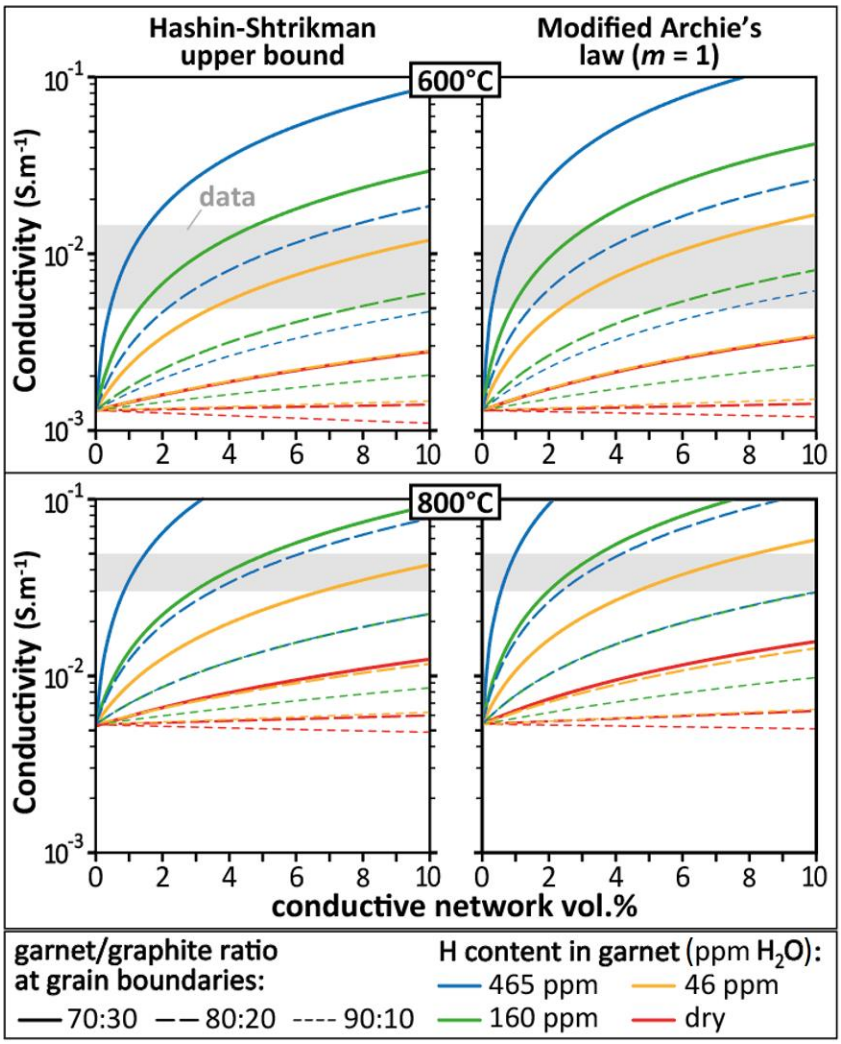

Figure 12: Effect of garnet/graphite ratio and H content on conductivity. Detailed simulations for the Hashin-Shtrikman upper bound (left) and the modified Archie's law (right) at 600 and 800°C. Simulation on ENG7 composition, compared to data (grey). The parameters used for the models are listed in **Table S3**. The formula are detailed in **Table S4**, with a table of values provided in **Table S5**.

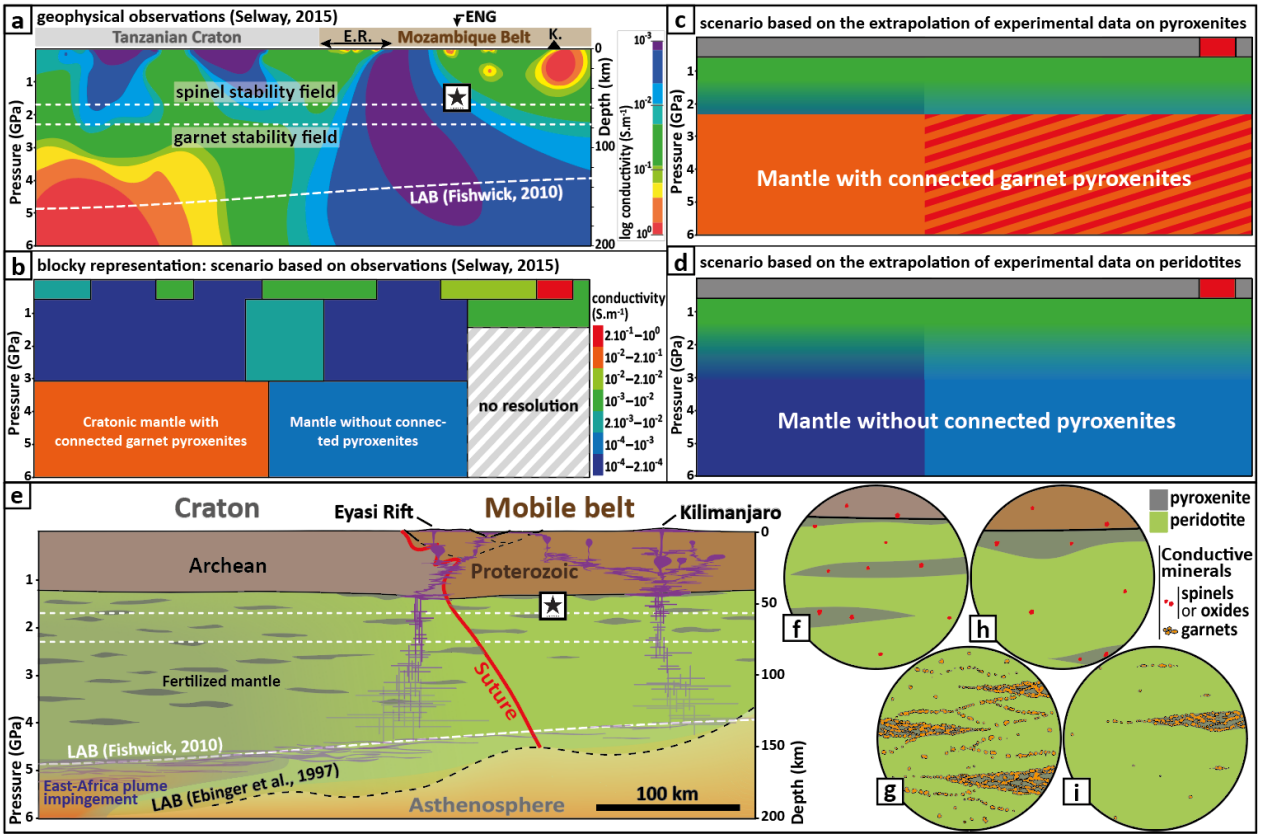

Figure 13: Geophysical and geological implications. (a) Results of the magnetotelluric survey (redrawn after Selway, 2015) located in **Fig.1**, with depth of the spinel-garnet transition (O'Hara et al., 1971) and LAB (Fishwisk, 2010); **(b)** Block representation of the best fit from connectivity data inversions (Selway, 2015); **(c)** block representation from the extrapolation of the experiments on pyroxenites; **(d)** block representation from the extrapolation of the experiments on pyroxenites; **(e)** Geological interpretation, with up-to-date topography (Wichura et al., 2011), Moho depth (Last et al., 1997; Julià et al., 2005), Lithosphere-Asthenosphere Boundary (LAB; Ebinger et al., 1997; Fishwick, 2010) and Eyasi suture zone (Ebinger et al., 1997) (vertical exaggeration x2). **f)** uppermost cratonic mantle at 1.5 GPa; **(g)** deep cratonic lithosphere containing a network of connected garnets; **(h)** uppermost mantle of the Mozambique Belt; **(i)** with limited garnet connectivity. The Blackstar indicates the approximate origin of the Engorora xenoliths (Chin, 2018), i.e. 0.9-1.7 GPa (**Fig.4**). Legend: ENG = Engorora; E.R = Eyasi Rift; K = Kilimanjaro.

References

1. Aines, R. D. & Rossman, G. R. 1984. Water content of mantle garnets. *Geology* **12**(12), 720-723.
2. Bizimis, M. & Peslier, A. H. 2015. Water in Hawaiian garnet pyroxenites: Implications for water heterogeneity in the mantle. *Chemical Geology* **397**, 61-75.
3. Celli, N. L., Lebedev, S., Schaeffer, A. J. & Gaina, C. 2020. African cratonic lithosphere carved by mantle plumes. *Nature Communications* **11**(1), 1-10.
4. Chin, E. J. 2018. Deep crustal cumulates reflect patterns of continental rift volcanism beneath Tanzania. *Contributions to Mineralogy & Petrology* **173**(10), 85.
5. Chin, E. J., Soustelle, V. & Liu, Y. 2020. An SPO-induced CPO in composite mantle xenoliths correlated with increasing melt-rock interaction. *Geochimica et Cosmochimica Acta* **278**, 199-218.
6. Chorowicz, J. 2005. The east African rift system. *Journal of African Earth Sciences* **43**(1-3), 379-410.
7. Clerc, J. P., Giraud, G., Alexander, S. & Guyon, E. 1979. Conductivity of a mixture of conducting and insulating grains: Dimensionality effects. *Physical Review B.* **22** (5): 2489-2494.
8. Dai, L., Li, H., Hu, H., Shan, S., Jiang, J. & Hui, K. 2012. The effect of chemical composition and oxygen fugacity on the electrical conductivity of dry and hydrous garnet at high temperatures and pressures. *Contributions to Mineralogy & Petrology* **163**(4), 689-700.
9. Dai, L. & Karato, S. I. 2009. Electrical conductivity of orthopyroxene: Implications for the water content of the asthenosphere. *Proceedings of the Japan Academy, Series B* **85**(10), 466-475.
10. Dawson, J. B., Powell, D. G. & Reid, A. M. 1970. Ultrabasic xenoliths and lava from the Lashaine volcano, northern Tanzania. *Journal of Petrology* **11**(3), 519-548.
11. Deldicque, D., Rouzaud, J. N., Vandevelde, S., Medina-Alcaide, M. Á., Ferrier, C., Perrenoud, C. ... & Cabanis, M. 2023. Effects of oxidative weathering on Raman spectra of charcoal and bone chars: consequences in archaeology and paleothermometry. *Comptes Rendus. Géoscience* **355**(G1), 1-22.
12. Doucet, L. S., Peslier, A. H., Ionov, D. A., Brandon, A. D., Golovin, A. V., Goncharov, A. G. & Ashchepkov, I. V. 2014. High water contents in the Siberian cratonic mantle linked to metasomatism: An FTIR study of Udachnaya peridotite xenoliths. *Geochimica et Cosmochimica Acta* **137**, 159-187.
13. Duba, A. G. & Shankland, T. J. 1982. Free carbon & electrical conductivity in the Earth's mantle. *Geophysical Research Letters* **9**(11), 1271-1274.
14. Ebinger, C., Djomani, Y. P., Mbede, E., Foster, A. & Dawson, J. B. 1997. Rifting archaean lithosphere: the Eyasi-Manyara-Natron rifts, East Africa. *Journal of the Geological Society* **154**(6), 947-960.
15. Evans, R. L., Jones, A. G., Garcia, X., Muller, M., Hamilton, M., Evans, S., ... & Hutchins, D. 2011. Electrical lithosphere beneath the Kaapvaal craton, southern Africa. *JGR Solid Earth* **116**(B4).
16. Ferrand, T. P. 2020. Conductive channels in the deep oceanic lithosphere could consist of garnet pyroxenites at the fossilized lithosphere–asthenosphere boundary. *Minerals* **10**(12), 1107.
17. Fisher, J. C. 1951. Calculation of diffusion penetration curves for surface and grain boundary diffusion. *Journal of Applied Physics* **22**(1), 74-77.
18. Fishwick, S. 2010. Surface wave tomography: imaging of the lithosphere–asthenosphere boundary beneath central and southern Africa? *Lithos* **120**(1-2), 63-73.
19. Foley, S. F. 2008. Rejuvenation and erosion of the cratonic lithosphere. *Nature geoscience* **1**(8), 503-510.
20. Frost, D. J. & McCammon, C. A. 2008. The redox state of Earth's mantle. *Annual Review of Earth & Planetary Sciences* **36**, 389-420.
21. Gardés, E., Gaillard, F. & Tarits, P. 2014. Toward a unified hydrous olivine electrical conductivity law. *Geochemistry, Geophysics, Geosystems* **15**(12), 4984-5000.

22. Glover, P. W., Hole, M. J. & Pous, J. 2000. A modified Archie's law for two conducting phases. *Earth & Planetary Science Letters* **180**(3-4), 369-383.
23. Green, D. H. & Hibberson, W. 1970. The instability of plagioclase in peridotite at high pressure. *Lithos* **3**(3), 209-221.
24. Griffin, W. L. & O'Reilly, S. Y. 2007. The earliest subcontinental lithospheric mantle. *Developments in Precambrian Geology* **15**, 1013-1035.
25. Griffin, W. L., O'Reilly, S. Y., Afonso, J. C. & Begg, G. C. 2009. The composition and evolution of lithospheric mantle: a re-evaluation and its tectonic implications. *Journal of Petrology* **50**(7), 1185-1204.
26. Gudfinnsson, G. H. & Presnall, D. C. 1996. Melting relations of model lherzolite in the system CaO-MgO-Al_2O_3-SiO_2 at 2.4-3.4 GPa and the generation of komatiites. *Journal of Geophysical Research: Solid Earth* **101**(B12), 27701-27709.
27. Gueguen, Y. & Dienes, J. 1989. Transport properties of rocks from statistics and percolation. *Mathematical geology* **21**(1), 1-13.
28. Hales, A. L. 1969. A seismic discontinuity in the lithosphere. *Earth & Planetary Science Letters* **7**(1), 44-46.
29. Henjes-Kunst, F. & Altherr, R. 1992. Metamorphic petrology of xenoliths from Kenya and northern Tanzania and implications for geotherms and lithospheric structures. *Journal of Petrology* **33**(5), 1125-1156.
30. Hirschmann, M. M., Tenner, T., Aubaud, C. & Withers, A. C. 2009. Dehydration melting of nominally anhydrous mantle: The primacy of partitioning. *PEPI* **176**(1-2), 54-68.
31. Hirth, G. & Kohlstedf, D. 2003. Rheology of the upper mantle and the mantle wedge: A view from the experimentalists. Geophysical Monograph – American Geophysical Union **138**, 83-106.
32. Hu, J., Liu, L., Faccenda, M., Zhou, Q., Fischer, K. M., Marshak, S. & Lundstrom, C. 2018. Modification of the Western Gondwana craton by plume-lithosphere interaction. *Nature Geoscience* **11**(3), 203-210.
33. Irving, A. J. 1974. Geochemical and high-pressure experimental studies of garnet pyroxenite and pyroxene granulite xenoliths from the Delegate basaltic pipes, Australia. *Journal of Petrology* **15**(1), 1-40.
34. James, D. E., Niu, F. & Rokosky, J. 2003. Crustal structure of the Kaapvaal craton and its significance for early crustal evolution. *Lithos* **71**(2-4), 413-429.
35. John, T., Scherer, E. E., Haase, K. & Schenk, V. 2004. Trace element fractionation during fluid-induced eclogitization in a subducting slab: trace element and Lu-Hf-Sm-Nd isotope systematics. *Earth & Planetary Science Letters* **227**(3-4), 441-456.
36. Jones, A. G., Fullea, J., Evans, R. L. & Muller, M. R. 2012. Water in cratonic lithosphere: Calibrating laboratory-determined models of electrical conductivity of mantle minerals using geophysical and petrological observations. *Geochemistry, Geophysics, Geosystems* **13**(6).
37. Julià, J., Ammon, C. J. & Nyblade, A. A. 2005. Evidence for mafic lower crust in Tanzania, East Africa, from joint inversion of receiver functions and Rayleigh wave dispersion velocities. *Geophysical Journal International* **162**(2), 555-569.
38. Keir, D., Bastow, I. D., Whaler, K. A., Daly, E., Cornwell, D. G. & Hautot, S. 2009. Lower crustal earthquakes near the Ethiopian rift induced by magmatic processes. *Geochemistry, Geophysics, Geosystems* **10**(6).
39. Keppler, H., Wiedenbeck, M. & Shcheka, S. S. 2003. Carbon solubility in olivine and the mode of carbon storage in the Earth's mantle. *Nature* **424**(6947), 414-416.

40. Kogiso, T., Hirschmann, M. M. & Frost, D. J. 2003. High-pressure partial melting of garnet pyroxenite: possible mafic lithologies in the source of ocean island basalts. *Earth & Planetary Science Letters* **216**(4), 603-617.
41. Koptev, A., Burov, E., Calais, E., Leroy, S., Gerya, T., Guillou-Frottier, L. & Cloetingh, S. 2016. Contrasted continental rifting via plume-craton interaction: Applications to Central East African Rift. *Geoscience Frontiers* **7**(2), 221-236.
42. Koptev, A., Calais, E., Burov, E., Leroy, S. & Gerya, T. 2018. Along-axis variations of rift width in a coupled lithosphere-mantle system, Application to East Africa. *Geophysical Research Letters* **45**(11), 5362-5370.
43. Lambart, S., Baker, M. B. & Stolper, E. M. 2016. The role of pyroxenite in basalt genesis: Melt-PX, a melting parameterization for mantle pyroxenites between 0.9 and 5 GPa. *JGR Solid Earth* **121**(8), 5708-5735.
44. Lanari, P. & Engi, M. 2017. Local bulk composition effects on metamorphic mineral assemblages. *Reviews in Mineralogy & Geochemistry* **83**(1), 55-102.
45. Last, R. J., Nyblade, A. A., Langston, C. A. & Owens, T. J. 1997. Crustal structure of the East African Plateau from receiver functions and Rayleigh wave phase velocities. *Journal of Geophysical Research: Solid Earth* **102**(B11), 24469-24483.
46. Lee, C. T. & Rudnick, R. L. 1999. Compositionally stratified cratonic lithosphere: petrology and geochemistry of peridotite xenoliths from the Labait tuff cone, Tanzania. In *Proceedings of the 7th international Kimberlite conference* (pp. 503-521).
47. Lemna, O. S., Stephenson, R. & Cornwell, D. G. 2019. The role of pre-existing Precambrian structures in the development of Rukwa Rift Basin, southwest Tanzania. *Journal of African Earth Sciences* **150**, 607-625.
48. Liu, J., Pearson, D. G., Wang, L. H., Mather, K. A., Kjarsgaard, B. A., Schaeffer, A. J., ... & Armstrong, J. P. 2021. Plume-driven recratonization of deep continental lithospheric mantle. *Nature* **592**(7856), 732-736.
49. Maldener, J., Hösch, A., Langer, K. & Rauch, F. 2003. Hydrogen in some natural garnets studied by nuclear reaction analysis and vibrational spectroscopy. *Physics & Chemistry of Minerals* **30**(6), 337-344.
50. Miller, K. J., Montési, L. G. & Zhu, W. L. 2015. Estimates of olivine-basaltic melt electrical conductivity using a digital rock physics approach. *Earth & Planetary Science Letters* **432**, 332-341.
51. Muirhead, J. D., Fischer, T. P., Oliva, S. J., Laizer, A., van Wijk, J., Currie, C. A., ... & Ebinger, C. J. 2020. Displaced cratonic mantle concentrates deep carbon during continental rifting. *Nature* **582**(7810), 67-72.
52. O'Donnell, J., Adams, A., Nyblade, A., Mulibo, G. & Tugume, F. 2013. The uppermost mantle shear wave velocity structure of eastern Africa from Rayleigh wave tomography: Constraints on rift evolution. *Geophysical Journal International* **194,** 961-978.
53. O'Hara, M. J., Richardson, S. W. & Wilson, G. 1971. Garnet-peridotite stability and occurrence in crust and mantle. *Contributions to Mineralogy & Petrology* **32**(1), 48-68.
54. O'Reilly, S. Y. & Griffin, W. L. 2013. Mantle metasomatism. *Metasomatism and the chemical transformation of rock*, 471-533.
55. Patro, P. K. & Sarma, S. V. S. 2009. Lithospheric electrical imaging of the Deccan trap covered region of western India. *Journal of Geophysical Research: Solid Earth* **114**(B1).

768 56. Pearson, D. G., Boyd, F. R., Haggerty, S. E., Pasteris, J. D., Field, S. W., Nixon, P. H. & Pokhilenko, N.
769 P. 1994. The characterisation and origin of graphite in cratonic lithospheric mantle: a petrological
770 carbon isotope and Raman spectroscopic study. *Contributions to Mineralogy & Petrology* **115**(4),
771 449-466.
772 57. Peslier, A. H., Schönbächler, M., Busemann, H. & Karato, S. I. 2017. Water in the Earth's interior:
773 Distribution and origin. *Space Science Reviews* **212**(1), 743-810.
774 58. Phethean, J. J., Kalnins, L. M., van Hunen, J., Biffi, P. G., Davies, R. J. & McCaffrey, K. J. 2016.
775 Madagascar's escape from Africa: A high-resolution plate reconstruction for the Western Somali
776 Basin and implications for supercontinent dispersal. *Geochemistry, Geophysics, Geosystems* **17**(12),
777 5036-5055.
778 59. Pommier, A. & Leinenweber, K. D. 2018. Electrical cell assembly for reproducible conductivity
779 experiments in the multi-anvil. *American Mineralogist* **103**(8), 1298-1305.
780 60. Ridley, J. & Thompson, A. 1986. The role of mineral kinetics in the development of metamorphic
781 microtextures. *Advances in physical geochemistry* **5**, 154-193.
782 61. Romano, C., Poe, B. T., Kreidie, N. & McCammon, C. A. 2006. Electrical conductivities of pyrope-
783 almandine garnets up to 19 GPa and 1700 C. *American Mineralogist* **91**(8-9), 1371-1377.
784 62. Rudnick, R. L., McDonough, W. F. & Chappell, B. W. 1993. Carbonatite metasomatism in the northern
785 Tanzanian mantle: petrographic and geochemical characteristics. *Earth & Planetary Science*
786 *Letters* **114**(4), 463-475.
787 63. Sarafian, E., Evans, R. L., Abdelsalam, M. G., Atekwana, E., Elsenbeck, J., Jones, A. G. & Chikambwe,
788 E. 2018. Imaging Precambrian lithospheric structure in Zambia using electromagnetic methods.
789 *Gondwana Research* **54**, 38-49.
790 64. Sleep, N. H. 1997. Lateral flow and ponding of starting plume material. *Journal of Geophysical*
791 *Research: Solid Earth* **102**(B5), 10001-10012.
792 65. Selway, K. 2015. Negligible effect of hydrogen content on plate strength in East Africa. *Nature*
793 *Geoscience* **8**(7), 543-546.
794 66. Selway, K., Yi, J. & Karato, S-I. 2014. Water content of the Tanzanian lithosphere from
795 magnetotelluric data: Implications for cratonic growth and stability. *Earth & Planetary Science*
796 *Letters* **388**, 175-186.
797 67. Spear, F. S. 2017. Garnet growth after overstepping. *Chemical Geology* **466**, 491-499.
798 68. Takahashi, E. 1990. Speculations on the Archean mantle: missing link between komatiite and
799 depleted garnet peridotite. *Journal of Geophysical Research: Solid Earth* **95**(B10), 15941-15954.
800 69. Vauchez, A., Dineur, F. & Rudnick, R. 2005. Microstructure, texture and seismic anisotropy of the
801 lithospheric mantle above a mantle plume: insights from the Labait volcano xenoliths (Tanzania).
802 *Earth & Planetary Science Letters* **232**(3-4), 295-314.
803 70. Vrijmoed, J. C., Austrheim, H., John, T., Hin, R. C., Corfu, F. & Davies, G. R. 2013. Metasomatism in
804 the ultrahigh-pressure Svartberget garnet-peridotite (Western Gneiss Region, Norway): implications
805 for the transport of crust-derived fluids within the mantle. *Journal of Petrology* **54**(9), 1815-1848.
806 71. Wang, D., Mookherjee, M., Xu, Y. & Karato, S. I. 2006. The effect of water on the electrical
807 conductivity of olivine. *Nature* **443**(7114), 977-980.
808 72. Wang, D., Li, H., Yi, L. & Shi, B. 2008. The electrical conductivity of upper-mantle rocks: water content
809 in the upper mantle. *Physics & Chemistry of Minerals* **35**(3), 157-162.
810 73. Wang, D., Karato, S. I. & Jiang, Z. 2013. An experimental study of the influence of graphite on the
811 electrical conductivity of olivine aggregates. *Geophysical Research Letters* **40**(10), 2028-2032.

74. Wang, H., van Hunen, J. & Pearson, D. G. 2015. The thinning of subcontinental lithosphere: The roles of plume impact and metasomatic weakening. *Geochemistry, Geophysics, Geosystems* **16**(4), 1156-1171.
75. Wang, L., Liu, J., Xu, Q. H. & Xia, Q. K. 2022. Craton destruction induced by drastic drops in lithospheric mantle viscosity. *Earth & Space Science*, e2022EA002455.
76. Wang, L., Hitchman, A. P., Ogawa, Y., Siripunvaraporn, W., Ichiki, M. & Fuji-ta, K. 2014. A 3-D conductivity model of the Australian continent using observatory and magnetometer array data. *Geophysical Journal International*, **198**(2), 1143-1158.
77. Watson, H. C., Roberts, J. J. & Tyburczy, J. A. 2010. Effect of conductive impurities on electrical conductivity in polycrystalline olivine. *Geophysical Research Letters* **37**(2).
78. Watson, E. B. 1986. Immobility of reduced carbon along grain boundaries in dunite. *Geophysical Research Letters* **13**(6), 529-532.
79. Wichura, H., Bousquet, R., Oberhänsli, R., Strecker, M. R. & Trauth, M. H. 2011. The Mid-Miocene East African Plateau: a pre-rift topographic model inferred from the emplacement of the phonolitic Yatta lava flow, Kenya. *Geological Society, London, Special Publications* **357**(1), 285-300.
80. Yang, X., Keppler, H., McCammon, C., Ni, H., Xia, Q. & Fan, Q. 2011. Effect of water on the electrical conductivity of lower crustal clinopyroxene. *Journal of Geophysical Research: Solid Earth* **116**(B4).
81. Ye, G., Unsworth, M., Wei, W., Jin, S. & Liu, Z. 2019. The Lithospheric Structure of the Solonker Suture Zone and Adjacent Areas: Crustal Anisotropy Revealed by a High-Resolution Magnetotelluric Study. *JGR Solid Earth* **124**(2), 1142-1163.
82. Yoshino, T., Shimojuku, A., Shan, S., Guo, X., Yamazaki, D., Ito, E., ... & Funakoshi, K. I. 2012. Effect of temperature, pressure and iron content on the electrical conductivity of olivine and its high-pressure polymorphs. *JGR Solid Earth* **117**(B8).
83. Zhang, B. & Yoshino, T. 2017. Effect of graphite on the electrical conductivity of the lithospheric mantle. *Geochemistry, Geophysics, Geosystems* **18**(1), 23-40.
84. Zhu, W., Gaetani, G. A., Fusseis, F., Montési, L. G. & De Carlo, F. 2011. Microtomography of partially molten rocks: three-dimensional melt distribution in mantle peridotite. *Science* **332**(6025), 88-91.